CHAPTER 3

ON THE REFLECTION OF THERMOELASTIC WAVES UNDER EXACT HEAT CONDUCTION MODEL WITH SINGLE DELAY

3.1 Introduction[1]

The study of wave propagation in a thermoelastic medium is a topic of great interest for researchers in the view of its several applications in the field of aeronautics, atomic physics, soil dynamics, thermal power plants, etc. The study of motion of thermoelastic waves is essential in geophysics, seismology, and mining as reflection and refraction techniques are used to study the composition and evolution of the Earth. Hence, study of reflection of waves has been a popular research area since 19th century. In 1899, Knott (1899) formulated the general equations of reflection and refraction of elastic waves at a plane half-space and studied the reflection and refraction of elastic waves by indicating its applications in seismology. Jeffreys (1930) and Gutenberg (1944) considered a solid half-space problem to study the reflection of elastic plane waves. Beevers and Bree (1975) examined linear coupled thermoelasticity theory on the basis of wave reflection problem. Reflection of thermoelastic waves in the context of GL thermoelasticity theory at a solid half-space was studied by Sinha and Elsibai (1996).

[1]The content of this chapter is under review in an international journal.

Singh (2003) explored the wave propagation for generalized thermoelasticity theory for anisotropic medium. Sharma et al. (2003) investigated reflection for thermoelastic waves for linear theories of thermoelasticity: LS theory, GL theory, GN theory, classical theory, and uncoupled theory. Kumar and Sarthi (2006) studied the reflection and refraction of thermoelastic plane waves at an interface for GN II theory. Othman and Song (2007) examined the reflection of thermoelastic waves in case of hydrostatic initial stress under GN thermoelasticity theory. Othman and Kumar (2009) analyzed the reflection of harmonic waves for generalized magneto-thermoelasticity theory. Singh (2010) studied the reflection of thermoelastic waves at thermally insulated stress-free boundary of monoclinic half-space. Kumar et al. (2014) elaborated the reflection process of thermoelastic waves with two temperatures and micropolar theory for GN model. Sarkar et al. (2019) analyzed reflection of thermoelastic plane waves under memory-dependent heat transfer theory. Deswal et al. (2019b) presented an analysis on the reflection of thermoelastic waves in the context of homogeneous, anisotropic, and fiber-reinforced thermoelastic rotating medium.

Processes at high temperature witness the dependence of material parameters on temperature (Noda (1986)), and considering variable material parameters makes the problem more realistic. Othman (2002) discussed about the effects of variable modulus of elasticity on two dimensional problem for generalized thermoelasticity whereas Youssef (2006a) reflected upon the effects of variable material parameters for generalized magneto-thermoelasticity. Analysis of reflection of magneto-thermoelastic waves in the context of Green-Lindsay theory with variable parameters was studied by Othman and Song (2008). Zenkour et al. (2013) worked upon the reflection of plane waves for dual-phase-lag thermoelasticity theory with variable material properties. Deswal et al. (2019a) analyzed reflection of plane waves under generalized thermoelasticity theory for fiber-reinforced medium with temperature-dependent properties.

In Chapter 2, the thermoelastic model based on exact heat conduction model with a

single delay term (Quintanilla (2011) and Leseduarte and Quintanilla (2013)) has been considered and after derivation of some important theorems, Galerkin-type representation of solution for a problem under this theory has been established. Now the behavior of thermoelastic waves under this new theory is worth to be investigated. Therefore, in this chapter, the reflection of plane waves, that is, transverse and longitudinal waves at the isothermal stress-free surface boundary of an isotropic medium with temperature-dependent elastic properties is inspected in the context of Quintanilla's thermoelasticity theory. The reflection of longitudinal elastic-mode wave and thermal-mode wave at the isothermal stress-free surface of a material with temperature-dependent elastic properties is studied in a detailed way. Two cases based on different incident plane waves, i.e., incident longitudinal wave and incident transverse wave, are analyzed to illustrate the reflection of waves in the context of the recently proposed thermoelastic model. In order to highlight the characteristic features of wave propagation under Quintanilla's model, a comparison of the present results is made with the corresponding results under other theories. Further, a detailed analysis of the effects of temperature-dependent material properties on the reflection of waves is attempted. The problem has therefore been studied by considering the combined constitutive relations and field equations for Quintanilla's thermoelasticity theory, Green-Naghdi (III) thermoelasticity theory, Lord-Shulman thermoelasticity theory, and classical thermoelasticity theory. Analytical results are derived in a unified way to represent the results under all four theories. The difference of Quintanilla's model with other theories in terms of amplitude ratios and phase velocities for various waves is depicted numerically and presented graphically. Numerical computations are carried out by considering a particular material (magnesium crystal) and variation in amplitude ratios with respect to different incident angles is shown graphically. Phase velocity profiles for various wave frequencies are also displayed. Effect of variable material parameters in the present context is highlighted with the graphical results by varying the empirical material constant. Several

important points arising out of the current investigation are highlighted.

3.2 Problem Formulation and Governing Equations

An isotropic thermoelastic medium half-space with elastic properties depending on temperature is considered to investigate the thermoelastic plane waves. The rectangular coordinate system (x, y, z) is considered such that the x-axis is along the surface of half-space with positive z-axis directed downwards into the half-space (Fig. 3.3.1). Further, for this analysis, plane strain is confined to the $xz-$plane, as a result, all the field variables are taken as functions of x, z, and t. Plane $z = 0$ is considered as the plane of incidence. Moreover, $\boldsymbol{u} = (u_1(x, z, t),\ 0,\ u_3(x, z, t))$ is taken as the displacement vector. Following the theories of generalized thermoelasticity given by Quintanilla (2011), Green-Naghdi (III) (1991), Lord-Shulman (1967), and Biot (1956), the combined equation of motion, heat conduction equation, and the stress-displacement relation, in the absence of body forces and heat sources, are respectively considered as follows:

$$(\lambda + \mu)\, \boldsymbol{\nabla}\, (\boldsymbol{\nabla}.\boldsymbol{u}) + \mu \nabla^2 \boldsymbol{u} - \beta \boldsymbol{\nabla}\theta = \rho \frac{\partial^2 \boldsymbol{u}}{\partial t^2}, \tag{3.2.1}$$

$$\left[K \frac{\partial}{\partial t} + K^* \left(1 - \tau \frac{\partial}{\partial t} + \frac{\tau^2}{2} \frac{\partial^2}{\partial t^2}\right)\right] \nabla^2 \theta = \left(\frac{\partial^2}{\partial t^2} + \tau_q \frac{\partial^3}{\partial t^3}\right) (\rho c_E \theta + \beta T_0 \boldsymbol{\nabla}.\boldsymbol{u}), \tag{3.2.2}$$

$$\boldsymbol{\Gamma} = \lambda (\boldsymbol{\nabla}.\boldsymbol{u})\, \boldsymbol{I} + \mu \left(\boldsymbol{\nabla u} + (\boldsymbol{\nabla u})^T\right) - \beta\, \theta\, \boldsymbol{I}. \tag{3.2.3}$$

where, τ represents delay time and $\boldsymbol{I}$ denotes the identity matrix of order three.
Equations (3.2.1–3.2.3) represent different thermoelasticity theories for the following values of material parameters:

- Quintanilla Model: $K^* \neq 0,\ \tau \neq 0,\ \tau_q = 0.$
- GN III Model: $K^* \neq 0,\ \tau = 0,\ \tau_q = 0.$
- Lord-Shulman Model: $K^* = \tau = 0,\ \tau_q \neq 0.$

- Biot's Model: $K^* = \tau = \tau_q = 0$.

Now, the elastic properties are assumed to be dependent on temperature by considering

$$\lambda = \lambda_0 f(\theta), \quad \mu = \mu_0 f(\theta), \quad \beta = \beta_0 f(\theta), \tag{3.2.4}$$

where, λ_0, μ_0, and β_0 are supposed as constants and $f(\theta)$ is the dimensionless function of temperature. Moreover, the scenario of temperature independent elastic material property will arise when $f(\theta) = 1$.

Using the Eq. (3.2.4) in Eqs. (3.2.1-3.2.3), gives

$$f(\theta)\left[(\lambda_0 + \mu_0)\,\boldsymbol{\nabla}\,(\boldsymbol{\nabla}.\boldsymbol{u}) + \mu_0 \nabla^2 \boldsymbol{u} - \beta_0 \boldsymbol{\nabla}\theta\right] = \rho \frac{\partial^2 \boldsymbol{u}}{\partial t^2}, \tag{3.2.5}$$

$$\left[K\frac{\partial}{\partial t} + K^*\left(1 - \tau\frac{\partial}{\partial t} + \frac{\tau^2}{2}\frac{\partial^2}{\partial t^2}\right)\right]\nabla^2\theta = \left(\frac{\partial^2}{\partial t^2} + \tau_q \frac{\partial^3}{\partial t^3}\right)\left(\rho c_E\,\theta + f(\theta)\beta_0 T_0 \boldsymbol{\nabla}.\boldsymbol{u}\right), \tag{3.2.6}$$

$$\boldsymbol{\Gamma} = f(\theta)\left[\lambda_0(\boldsymbol{\nabla}.\boldsymbol{u})\,\boldsymbol{I} + \mu_0\left(\boldsymbol{\nabla}\boldsymbol{u} + (\boldsymbol{\nabla}\boldsymbol{u})^T\right) - \beta_0\,\theta\,\boldsymbol{I}\right]. \tag{3.2.7}$$

Further, $f(\theta)$ is taken as a linear empirical relation in temperature (θ) to analyze the temperature dependency of elastic properties. Therefore, the following is considered:

$$f(\theta) = 1 - \alpha^*(\theta), \tag{3.2.8}$$

where, α^* is called the empirical material constant or non-homogeneity index parameter. Moreover, in order to form linear governing partial differential equations of the problem, it must be assumed that $|\theta|/T_0 = 1$, which gives the estimation of the function $f(\theta)$ as

$$f(\theta) = 1 - \alpha^* T_0. \tag{3.2.9}$$

Hence, the Eqs. (3.2.5-3.2.7) transform to:

$$(1-\alpha^* T_0)\left[(\lambda_0+\mu_0)\,\boldsymbol{\nabla}\,(\boldsymbol{\nabla}.\boldsymbol{u})+\mu_0\nabla^2\boldsymbol{u}-\beta_0\boldsymbol{\nabla}\theta\right]=\rho\frac{\partial^2\boldsymbol{u}}{\partial t^2}, \tag{3.2.10}$$

$$\left[K\frac{\partial}{\partial t}+K^*\left(1-\tau\frac{\partial}{\partial t}+\frac{\tau^2}{2}\frac{\partial^2}{\partial t^2}\right)\right]\nabla^2\theta=\left(\frac{\partial^2}{\partial t^2}+\tau_q\frac{\partial^3}{\partial t^3}\right)\left(\rho c_E\theta+(1-\alpha^* T_0)\,\beta_0 T_0\boldsymbol{\nabla}.\boldsymbol{u}\right), \tag{3.2.11}$$

$$\boldsymbol{\Gamma}=(1-\alpha^* T_0)\left[\lambda_0(\boldsymbol{\nabla}.\boldsymbol{u})\,\boldsymbol{I}+\mu_0\left(\boldsymbol{\nabla}\boldsymbol{u}+(\boldsymbol{\nabla}\boldsymbol{u})^T\right)-\beta_0\,\theta\,\boldsymbol{I}\right]. \tag{3.2.12}$$

For simplifying the calculations, the following dimensionless quantities are introduced in the system of Eqs. (3.2.10-3.2.12):

$$x'=\frac{x}{l},\quad z,=\frac{z}{l},\quad \theta'=\frac{\theta}{T_0},\quad t'=\frac{\nu t}{l},\quad \tau_q'=\frac{\nu\tau_q}{l},\quad \tau'=\frac{\nu\tau}{l},$$
$$\boldsymbol{\Gamma}'=\frac{\boldsymbol{\Gamma}}{\beta_0 T_0},\quad u_1'=\frac{(\lambda_0+2\mu_0)\,u_1}{l\beta_0 T_0},\quad u_3'=\frac{(\lambda_0+2\mu_0)\,u_3}{l\beta_0 T_0},$$

where, l and v denotes standard length and velocity. Dropping the prime for convenience, the Eqs. (3.2.10-3.2.12) reform as follows:

$$\left[\left(C_1^2-C_2^2\right)\boldsymbol{\nabla}\,(\boldsymbol{\nabla}.\boldsymbol{u})+C_2^2\nabla^2\boldsymbol{u}-C_1^2\boldsymbol{\nabla}\theta\right]=\alpha_1\frac{\partial^2\boldsymbol{u}}{\partial t^2}, \tag{3.2.13}$$

$$\left[C_4^2\frac{\partial}{\partial t}+C_3^2\left(1-\tau\frac{\partial}{\partial t}+\frac{\tau^2}{2}\frac{\partial^2}{\partial t^2}\right)\right]\nabla^2\theta=\left(\frac{\partial^2}{\partial t^2}+\tau_q\frac{\partial^3}{\partial t^3}\right)\left(\theta+\frac{\epsilon}{\alpha_1}\boldsymbol{\nabla}.\boldsymbol{u}\right), \tag{3.2.14}$$

$$\boldsymbol{\Gamma}=\frac{1}{\alpha_1}\left[\left(1-\frac{2C_2^2}{C_1^2}\right)(\boldsymbol{\nabla}.\boldsymbol{u})\,\boldsymbol{I}+\frac{2C_2^2}{C_1^2}\left(\boldsymbol{\nabla}\boldsymbol{u}+(\boldsymbol{\nabla}\boldsymbol{u})^T\right)-\theta\,\boldsymbol{I}\right], \tag{3.2.15}$$

where,

$$C_1^2=\frac{\lambda_0+2\mu_0}{\rho\nu^2},\ C_2^2=\frac{\mu_0}{\rho\nu^2},\ C_3^2=\frac{K_0^*}{\rho c_E\nu^2},\ C_4^2=\frac{K_0^*}{\rho c_E\nu l},\ \epsilon=\frac{\beta_0^2 T_0}{\rho c_E(\lambda_0+2\mu_0)},\ \alpha=\frac{1}{1-\alpha^* T_0}.$$

Now, with the help of Helmholtz's representation, the displacement vector can be decomposed in terms of scalar and vector potential functions, ϕ and $\boldsymbol{\psi}$, respectively. The scalar function corresponds to longitudinal wave, in which motion of particles is in the direction of wave propagation. On the other hand, vector potential function represents transverse wave, in which motion of particle is perpendicular to the direction of wave

propagation. Therefore, the following form is taken:

$$\boldsymbol{u} = \boldsymbol{\nabla}\phi + \boldsymbol{\nabla} \times \boldsymbol{\psi}, \quad \boldsymbol{\nabla}.\boldsymbol{\psi} = 0. \tag{3.2.16}$$

Substituting (3.2.16) in Eq. (3.2.13) and Eq. (3.2.14), the following is acquired:

$$\begin{aligned}\left[\left(C_1^2 - C_2^2\right)\boldsymbol{\nabla}\left(\boldsymbol{\nabla}.\left(\boldsymbol{\nabla}\phi + \boldsymbol{\nabla} \times \boldsymbol{\psi}\right)\right) + C_2^2\nabla^2\left(\boldsymbol{\nabla}\phi + \boldsymbol{\nabla} \times \boldsymbol{\psi}\right) - C_1^2\boldsymbol{\nabla}\theta\right] \\ = \alpha_1\frac{\partial^2}{\partial t^2}\left(\boldsymbol{\nabla}\phi + \boldsymbol{\nabla} \times \boldsymbol{\psi}\right),\end{aligned} \tag{3.2.17}$$

$$\left[C_4^2\frac{\partial}{\partial t} + C_3^2\left(1 - \tau\frac{\partial}{\partial t} + \frac{\tau^2}{2}\frac{\partial^2}{\partial t^2}\right)\right]\nabla^2\theta = \left(\frac{\partial^2}{\partial t^2} + \tau_q\frac{\partial^3}{\partial t^3}\right)\left(\theta + \frac{\epsilon}{\alpha_1}\boldsymbol{\nabla}.\left(\boldsymbol{\nabla}\phi + \boldsymbol{\nabla} \times \boldsymbol{\psi}\right)\right). \tag{3.2.18}$$

The above equations can be rewritten as

$$\boldsymbol{\nabla}\left(C_1^2\nabla^2\phi - \alpha_1\frac{\partial^2\phi}{\partial t^2} - C_1^2\theta\right) + \boldsymbol{\nabla} \times \left(C_2^2\nabla^2\boldsymbol{\psi} - \alpha_1\frac{\partial^2\boldsymbol{\psi}}{\partial t^2}\right) = 0, \tag{3.2.19}$$

$$\left[C_4^2\frac{\partial}{\partial t} + C_3^2\left(1 - \tau\frac{\partial}{\partial t} + \frac{\tau^2}{2}\frac{\partial^2}{\partial t^2}\right)\right]\nabla^2\theta = \left(\frac{\partial^2}{\partial t^2} + \tau_q\frac{\partial^3}{\partial t^3}\right)\left(\theta + \frac{\epsilon}{\alpha_1}\nabla^2\phi\right). \tag{3.2.20}$$

Clearly, Eq. (3.2.19) will be satisfied if the following conditions are satisfied:

$$\nabla^2\phi - \frac{\alpha_1}{C_1^2}\frac{\partial^2\phi}{\partial t^2} = \theta, \tag{3.2.21}$$

and

$$\nabla^2\boldsymbol{\psi} - \frac{\alpha_1}{C_2^2}\frac{\partial^2\boldsymbol{\psi}}{\partial t^2} = 0. \tag{3.2.22}$$

Further, as the plain strain is assumed to be restricted to xz–plane, $\boldsymbol{\psi} = (0, \psi_2, 0)$ is considered as the potential function corresponding to transverse wave. Hence, the Eq. (3.2.22) transforms to

$$\nabla^2\psi_2 - \frac{\alpha_1}{C_2^2}\frac{\partial^2\psi_2}{\partial t^2} = 0. \tag{3.2.23}$$

It is observed that longitudinal wave is affected by thermal field as the Eq. (3.2.20) and Eq. (3.2.21) involve both ϕ and θ. Hence, the Eq. (3.2.20) and Eq. (3.2.21) are

coupled partial differential equations. However, Eq. (3.2.23) contains only ψ_2 which implies that the transverse wave remains unaffected of thermal field.

Now, eliminating θ from Eq. (3.2.20) and Eq. (3.2.21) gives

$$\left[C_4^2\frac{\partial}{\partial t}+C_3^2\left(1-\tau\frac{\partial}{\partial t}+\frac{\tau^2}{2}\frac{\partial^2}{\partial t^2}\right)\right]\nabla^4\phi-\left[\frac{\alpha_1}{C_1^2}\frac{\partial^2}{\partial t^2}\left(C_4^2\frac{\partial}{\partial t}+C_3^2\left(1-\tau\frac{\partial}{\partial t}+\frac{\tau^2}{2}\frac{\partial^2}{\partial t^2}\right)\right)\right.$$
$$\left.+\left(1+\frac{\epsilon}{\alpha_1}\right)\left(\frac{\partial^2}{\partial t^2}+\tau_q\frac{\partial^3}{\partial t^3}\right)\right]\nabla^2\phi+\frac{\alpha_1}{C_1^2}\left(\frac{\partial^4\phi}{\partial t^4}+\tau_q\frac{\partial^5\phi}{\partial t^5}\right)=0. \tag{3.2.24}$$

Moreover, in terms of potential functions, the displacement, and stress components can be expressed as:

$$u_1=\frac{\partial\phi}{\partial x}-\frac{\partial\psi_2}{\partial z},\quad u_2=0,\quad u_3=\frac{\partial\phi}{\partial z}+\frac{\partial\psi_2}{\partial x}, \tag{3.2.25}$$

$$\sigma_{zz}=\frac{1}{\alpha_1}\left[\frac{\partial^2\phi}{\partial x^2}+\frac{\partial^2\phi}{\partial z^2}+\frac{2C_2^2}{C_1^2}\left(\frac{\partial^2\psi_2}{\partial x\partial z}-\frac{\partial^2\phi}{\partial x^2}\right)-\theta\right], \tag{3.2.26}$$

$$\sigma_{xz}=\frac{C_2^2}{\alpha_1C_1^2}\left[2\frac{\partial^2\phi}{\partial x\partial z}+\frac{\partial^2\psi_2}{\partial x^2}-\frac{\partial^2\psi_2}{\partial z^2}\right]. \tag{3.2.27}$$

Now, on the surface $z=0$ of half space, the non-dimensional boundary conditions are considered as follows:

- Stress-free surface

$$\sigma_{zz}=\sigma_{xz}=0,\quad \text{at } z=0. \tag{3.2.28}$$

- Isothermal surface

$$\theta=0,\quad \text{at } z=0. \tag{3.2.29}$$

3.3 Solution of the Problem

In order to analyze the harmonic wave propagation, the direction of wave is supposed such that normal to the wave falls in the $xz-$plane and forms an angle ζ with the $z-$axis. For this purpose, the solution for displacement potential function, ϕ is supposed

to be in the following form:

$$\phi = \mathfrak{A}\exp(\mathrm{i}\gamma\,(x\sin\zeta - z\cos\zeta) - \mathrm{i}\omega t), \tag{3.3.1}$$

where, ω is the complex circular frequency, γ is the wave number, $\mathrm{i} = \sqrt{-1}$, and $(\sin\,\zeta, \cos\,\zeta)$ represents the projection of the wave normal onto $xz-$plane with $\mathfrak{A}$ as an arbitrary constant.

Now, using Eq. (3.2.24) and Eq. (3.3.1), the quadratic equation in γ^2 is obtained as

$$L\gamma^4 - M\gamma^2 + N = 0, \tag{3.3.2}$$

where,

$$\begin{aligned}
L &= -\mathrm{i}C_4^2\omega + C_3^2\left(1 + \mathrm{i}\tau\omega - \frac{\tau^2}{2}\omega^2\right),\\
M &= \frac{\alpha_1}{C_1^2}\left(-C_4^2\mathrm{i}\omega^3 + C_3^2\left(\omega^2 + \mathrm{i}\tau\omega^3 - \frac{\tau^2}{2}\omega^4\right)\right) - \left(1 + \frac{\epsilon}{\alpha_1}\right)(-\omega^2 + \mathrm{i}\tau_q\omega^3),\\
N &= \frac{\alpha_1}{C_1^2}(\omega^4 - \mathrm{i}\tau_q\omega^5).
\end{aligned}$$

Solving Eq. (3.3.2), the two roots γ_1^2 and γ_2^2 are acquired as

$$\gamma_{1,2}^2 = \frac{1}{2L}\left(M \mp \sqrt{M^2 - 4LN}\right), \tag{3.3.3}$$

where, γ_1 and γ_2 are the wave numbers corresponding to elastic-mode longitudinal wave and thermal-mode wave, respectively with $V_1 = \frac{\omega}{\mathrm{Re}[\gamma_1]}$ and $V_2 = \frac{\omega}{\mathrm{Re}[\gamma_2]}$ as phase velocities.

Similarly, the solution of Eq. (3.2.23) can be assumed as

$$\psi_2 = \mathfrak{B}\exp(\mathrm{i}\gamma_3\,(x\sin\zeta - z\cos\zeta) - \mathrm{i}\omega t), \tag{3.3.4}$$

where,$\mathfrak{B}$ is an arbitrary constant and $\gamma_3^2 = \frac{\alpha_1\omega^2}{C_2^2}$ is the wave number corresponding to elastic-mode transverse wave with $V_3 = \frac{\omega}{\mathrm{Re}[\gamma_3]}$ as phase velocity.

3.3.1 Case A: Incident Longitudinal Wave

As discussed earlier, there are two types of wave, namely, longitudinal wave and transverse wave. Therefore, to analyze the reflection of thermoelastic waves , two cases are discussed on this basis. Firstly, the scenario is discussed when the longitudinal wave falls at the surface (Case A) and secondly, when the incident transverse wave falls at the surface (Case B).

This is the case when from within the elastic medium, a longitudinal wave incidence on the boundary $z = 0$, making an angle ζ_0 with the direction of the $z-$axis, then the displacement potentials ϕ and ψ can be taken in the following form (after subsiding the time harmonic factor $\exp(-\mathrm{i}\omega t)$):

$$\phi = \mathfrak{A}_1 \exp(\mathrm{i}\gamma_1 (x\sin\zeta_0 - z\cos\zeta_0)) + \mathfrak{A}_2 \exp(\mathrm{i}\gamma_1 (x\sin\zeta_1 + z\cos\zeta_1)) + \mathfrak{A}_3 \exp(\mathrm{i}\gamma_2 (x\sin\zeta_2 + z\cos\zeta_2)), \tag{3.3.5}$$

$$\psi_2 = \mathfrak{A}_4 \exp(\mathrm{i}\gamma_3 (x\sin\zeta_3 + z\cos\zeta_3)), \tag{3.3.6}$$

where, $\mathfrak{A}_1$ represents the amplitude of the incident longitudinal wave, and $\mathfrak{A}_2$, $\mathfrak{A}_3$, $\mathfrak{A}_4$ are the amplitudes of the reflected longitudinal wave, reflected thermal-mode wave and reflected transverse wave, respectively. Also, ζ_0, ζ_1, ζ_2, and ζ_3 are the angles made by incident wave, reflected longitudinal wave, reflected thermal-mode wave, and reflected transverse wave with $z-$axis, respectively as shown in Fig. 3.3.1.

Therefore, in view of Eq. (3.2.21) and Eq. (3.3.5), temperature θ can be expressed as

$$\theta = b_1\mathfrak{A}_1 \exp(\mathrm{i}\gamma_1 (x\sin\zeta_0 - z\cos\zeta_0)) + b_1\mathfrak{A}_2 \exp(\mathrm{i}\gamma_1 (x\sin\zeta_1 + z\cos\zeta_1)) + b_2\mathfrak{A}_3 \exp(\mathrm{i}\gamma_2 (x\sin\zeta_2 + z\cos\zeta_2)), \tag{3.3.7}$$

where,

$$b_1 = \frac{\alpha_1}{C_1^2}\omega^2 - \gamma_1^2, \quad b_2 = \frac{\alpha_1}{C_1^2}\omega^2 - \gamma_2^2. \tag{3.3.8}$$

The reflection coefficient (amplitude ratio) is used to determine the reflected wave in terms of incident wave. It is therefore, defined as the ratio of amplitude of the reflected waves to the amplitude of the incident wave. Hence, $\frac{\mathfrak{A}_2}{\mathfrak{A}_1}$, $\frac{\mathfrak{A}_3}{\mathfrak{A}_1}$, and $\frac{\mathfrak{A}_4}{\mathfrak{A}_1}$ are the reflection coefficient of longitudinal elastic-mode wave, thermal-mode wave, and transverse elastic-mode wave, respectively.

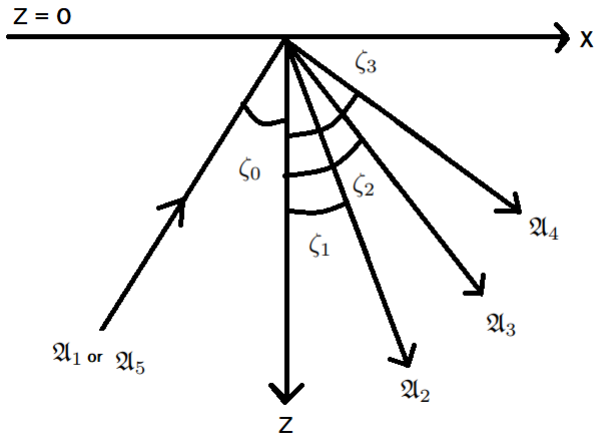

Figure 3.3.1: Geometry of the problem

Substituting the expression of potential functions presented by Eqs. (3.3.5-3.3.7) in Eqs. (3.2.26-3.2.27) and employing conditions at boundary, i.e., (3.2.28) and (3.2.29), yields

$$
\begin{aligned}
&-\mathfrak{A}_1\gamma_1^2\exp\left(\mathrm{i}\gamma_1 x\sin\zeta_0\right)-\mathfrak{A}_2\gamma_1^2\exp\left(\mathrm{i}\gamma_1 x\sin\zeta_1\right)-\mathfrak{A}_3\gamma_2^2\exp\left(\mathrm{i}\gamma_2 x\sin\zeta_2\right)\\
&+\frac{2C_2^2}{C_1^2}\left[-\mathfrak{A}_4\gamma_3^2\sin\zeta_3\cos\zeta_3\exp\left(\mathrm{i}\gamma_3 x\sin\zeta_3\right)+\mathfrak{A}_1\gamma_1^2\sin^2\zeta_0\exp\left(\mathrm{i}\gamma_1 x\sin\zeta_0\right)\right.\\
&\left.+\mathfrak{A}_2\gamma_1^2\sin^2\zeta_1\exp\left(\mathrm{i}\gamma_1 x\sin\zeta_1\right)+\mathfrak{A}_3\gamma_2^2\sin^2\zeta_2\exp\left(\mathrm{i}\gamma_2 x\sin\zeta_2\right)\right]-b_1\mathfrak{A}_1\exp\left(\mathrm{i}\gamma_1 x\sin\zeta_0\right)\\
&-b_1\mathfrak{A}_2\exp\left(\mathrm{i}\gamma_1 x\sin\zeta_1\right)-b_2\mathfrak{A}_3\exp\left(\mathrm{i}\gamma_2 x\sin\zeta_2\right)=0, \qquad (3.3.9)
\end{aligned}
$$

$$\mathfrak{A}_1\gamma_1^2\sin(2\zeta_0)\exp\left(\mathrm{i}\gamma_1 x\sin\zeta_0\right) - \mathfrak{A}_2\gamma_1^2\sin(2\zeta_1)\exp\left(\mathrm{i}\gamma_1 x\sin\zeta_1\right)$$
$$-\mathfrak{A}_3\gamma_2^2\sin(2\zeta_2)\exp\left(\mathrm{i}\gamma_2 x\sin\zeta_2\right) + \mathfrak{A}_4\gamma_3^2\cos(2\zeta_3)\exp\left(\mathrm{i}\gamma_3 x\sin\zeta_3\right) = 0, \tag{3.3.10}$$

$$b_1\mathfrak{A}_1\exp\left(\mathrm{i}\gamma_1 x\sin\zeta_0\right) + b_1\mathfrak{A}_2\exp\left(\mathrm{i}\gamma_1 x\sin\zeta_1\right) + b_2\mathfrak{A}_3\exp\left(\mathrm{i}\gamma_2 x\sin\zeta_2\right) = 0. \tag{3.3.11}$$

Further, Eqs. (3.3.9-3.3.11) will hold for all values of x, if the following condition is satisfied:

$$\gamma_1\sin\zeta_0 = \gamma_1\sin\zeta_1 = \gamma_2\sin\zeta_2 = \gamma_3\sin\zeta_3. \tag{3.3.12}$$

This relation further implies that

$$\zeta_0 = \zeta_1 \quad \text{and } \sin\zeta_0 = \frac{\gamma_2}{\gamma_1}\sin\zeta_2 = \frac{\gamma_3}{\gamma_1}\sin\zeta_3, \tag{3.3.13}$$

which can be rewritten as

$$\zeta_0 = \zeta_1 \quad \text{and } \sin\zeta_0 = \frac{V_1}{V_2}\sin\zeta_2 = \frac{V_1}{V_3}\sin\zeta_3, \tag{3.3.14}$$

which is known as extended Snell's law.

In view of condition (3.3.14), Eqs. (3.3.9-3.3.11) constitute a system of three non-homogeneous equations in the four unknowns $\mathfrak{A}_1$, $\mathfrak{A}_2$, $\mathfrak{A}_3$, and $\mathfrak{A}_4$. Hence, solving equations for ratios of amplitudes $\frac{\mathfrak{A}_2}{\mathfrak{A}_1}$, $\frac{\mathfrak{A}_3}{\mathfrak{A}_1}$, and $\frac{\mathfrak{A}_4}{\mathfrak{A}_1}$ of the waves.

Matrix representation of Eqs. (3.3.9-3.3.11) can be written in the following form:

$$\begin{bmatrix} a_{11} & a_{12} & a_{13} \\ a_{21} & a_{22} & a_{23} \\ a_{31} & a_{32} & a_{33} \end{bmatrix} \begin{bmatrix} \mathfrak{A}_2/\mathfrak{A}_1 \\ \mathfrak{A}_3/\mathfrak{A}_1 \\ \mathfrak{A}_4/\mathfrak{A}_1 \end{bmatrix} = \begin{bmatrix} d_1 \\ d_2 \\ d_3 \end{bmatrix}, \tag{3.3.15}$$

where,

$$a_{11} = \frac{2C_2^2}{C_1^2}\gamma_1^2 \sin^2\zeta_1 - \frac{\alpha_1}{C_1^2}\omega^2, \quad a_{12} = \frac{2C_2^2}{C_1^2}\gamma_2^2 \sin^2\zeta_2 - \frac{\alpha_1}{C_1^2}\omega^2, \quad a_{13} = -\frac{C_2^2}{C_1^2}\gamma_3^2 \sin(2\zeta_3),$$

$$a_{21} = -\gamma_1^2 \sin(2\zeta_1), \quad a_{22} = -\gamma_2^2 \sin(2\zeta_2), \quad a_{23} = \gamma_3^2 \cos(2\zeta_3),$$

$$a_{31} = b_1, \quad , a_{32} = b_2, \quad , a_{33} = 0,$$

$$d_1 = \frac{\alpha_1}{C_1^2}\omega^2 - \frac{2C_2^2}{C_1^2}\gamma_1^2 \sin^2\zeta_0, \quad , d_2 = -\gamma_1^2 \sin(2\zeta_0), \quad d_3 = -b_1.$$

Using Cramer's rule, the solution for reflection coefficients is given by

$$Z_1 = \frac{\mathfrak{A}_2}{\mathfrak{A}_1} = \frac{\Delta_1}{\Delta}, \quad Z_2 = \frac{\mathfrak{A}_3}{\mathfrak{A}_1} = \frac{\Delta_2}{\Delta}, \quad Z_3 = \frac{\mathfrak{A}_4}{\mathfrak{A}_1} = \frac{\Delta_3}{\Delta}, \tag{3.3.16}$$

where,

$$\Delta = a_{11}(a_{22}a_{33} - a_{23}a_{32}) - a_{12}(a_{21}a_{33} - a_{23}a_{31}) + a_{13}(a_{21}a_{32} - a_{22}a_{31}),$$

$$\Delta_1 = d_1(a_{22}a_{33} - a_{23}a_{32}) - d_2(a_{12}a_{33} - a_{13}a_{32}) + d_3(a_{12}a_{23} - a_{13}a_{22}),$$

$$\Delta_2 = -d_1(a_{21}a_{33} - a_{23}a_{31}) + d_2(a_{11}a_{33} - a_{13}a_{31}) - d_3(a_{11}a_{23} - a_{13}a_{21}),$$

$$\Delta_3 = d_1(a_{21}a_{32} - a_{22}a_{31}) - d_2(a_{11}a_{32} - a_{12}a_{31}) + d_3(a_{11}a_{22} - a_{21}a_{12}).$$

Hence, the respective reflection coefficients of reflected longitudinal wave, reflected thermal-mode wave and reflected transverse wave are represented by the quantities Z_1, Z_2, and Z_3. Also, from the Eq. (3.3.16), it is observed that each reflective coefficient is dependent on wave characteristics of all the three waves. The reflection coefficients under different theories considered here can be obtained for various values of parameters as described in Section 3.2.

3.3.2 Case B: Incident Transverse Wave

Now in case of incident transverse wave, the displacement potentials, ϕ and ψ_2 and temperature, θ can be documented as follows (after omitting the harmonic time factor

$\exp(-\mathrm{i}\omega t)$):

$$\psi_2 = \mathfrak{A}_5 \exp(\mathrm{i}\gamma_3 (x\sin\zeta_0 - z\cos\zeta_0)) + \mathfrak{A}_4 \exp(\mathrm{i}\gamma_3 (x\sin\zeta_3 + z\cos\zeta_3)), \tag{3.3.17}$$

$$\phi = \mathfrak{A}_2 \exp(\mathrm{i}\gamma_1 (x\sin\zeta_1 + z\cos\zeta_1)) + \mathfrak{A}_3 \exp(\mathrm{i}\gamma_2 (x\sin\zeta_2 + z\cos\zeta_2)), \tag{3.3.18}$$

$$\theta = b_1\mathfrak{A}_2 \exp(\mathrm{i}\gamma_1 (x\sin\zeta_1 + z\cos\zeta_1)) + b_2\mathfrak{A}_3 \exp(\mathrm{i}\gamma_2 (x\sin\zeta_2 + z\cos\zeta_2)), \tag{3.3.19}$$

where, the amplitude of the incident transverse elastic-mode wave is represented by $\mathfrak{A}_5$. Now, plugging the expression of potential function presented by Eqs. (3.3.17-3.3.19) in Eqs. (3.2.26-3.2.27) and applying conditions at the boundary, i.e., (3.2.28) and (3.2.29), generates

$$\begin{aligned} &-\mathfrak{A}_2(\gamma_1^2 + b_1)\exp(\mathrm{i}\gamma_1 x\sin\zeta_1) - \mathfrak{A}_3(\gamma_2^2 + b_2)\exp(\mathrm{i}\gamma_2 x\sin\zeta_2) \\ &+\frac{2C_2^2}{C_1^2}\Big(\mathfrak{A}_5\gamma_3^2\sin\zeta_0\cos\zeta_0\exp(\mathrm{i}\gamma_3 x\sin\zeta_0) - \mathfrak{A}_4\gamma_3^2\sin\zeta_3\cos\zeta_3\exp(\mathrm{i}\gamma_3 x\sin\zeta_3) \\ &+\mathfrak{A}_2\gamma_1^2\sin^2\zeta_2\exp(\mathrm{i}\gamma_1 x\sin\zeta_1) + \mathfrak{A}_3\gamma_2^2\sin^2\zeta_3\exp(\mathrm{i}\gamma_2 x\sin\zeta_2)\Big) = 0, \end{aligned} \tag{3.3.20}$$

$$\begin{aligned} &-\mathfrak{A}_2\gamma_1^2\sin(2\zeta_1)\exp(\mathrm{i}\gamma_1 x\sin\zeta_1) - \mathfrak{A}_3\gamma_2^2\sin(2\zeta_2)\exp(\mathrm{i}\gamma_2 x\sin\zeta_2) \\ &+\mathfrak{A}_4\gamma_3^2\cos(2\zeta_3)\exp(\mathrm{i}\gamma_3 x\sin\zeta_3) + \mathfrak{A}_5\gamma_3^2\cos(2\zeta_0)\exp(\mathrm{i}\gamma_3 x\sin\zeta_0) = 0, \end{aligned} \tag{3.3.21}$$

$$b_1\mathfrak{A}_2\exp(\mathrm{i}\gamma_1 x\sin\zeta_1) + b_2\mathfrak{A}_3\exp(\mathrm{i}\gamma_2 x\sin\zeta_2) = 0. \tag{3.3.22}$$

Similar to the previous case, the above equations will hold if the following condition is satisfied

$$\gamma_3\sin\zeta_0 = \gamma_3\sin\zeta_3 = \gamma_1\sin\zeta_1 = \gamma_2\sin\zeta_2, \tag{3.3.23}$$

which further implies

$$\zeta_0 = \zeta_3 \quad \text{and} \quad \sin\zeta_0 = \frac{\gamma_1}{\gamma_3}\sin\zeta_1 = \frac{\gamma_2}{\gamma_3}\sin\zeta_2,$$

that finally gives extended Snell's law as

$$\zeta_0 = \zeta_3 \quad \text{and } \sin\,\zeta_0 = \frac{V_3}{V_1}\sin\zeta_1 = \frac{V_3}{V_2}\sin\zeta_2.$$

Similar to Case A, the above system of equations be represented as follows:

$$\begin{bmatrix} c_{11} & c_{12} & c_{13} \\ c_{21} & c_{22} & c_{23} \\ c_{31} & c_{32} & c_{33} \end{bmatrix} \begin{bmatrix} \mathfrak{A}_2/\mathfrak{A}_5 \\ \mathfrak{A}_3/\mathfrak{A}_5 \\ \mathfrak{A}_4/\mathfrak{A}_5 \end{bmatrix} = \begin{bmatrix} g_1 \\ g_2 \\ g_3 \end{bmatrix}, \tag{3.3.24}$$

where,

$$c_{11} = \frac{2C_2^2}{C_1^2}\gamma_1^2\sin^2\zeta_1 - \frac{\alpha_1}{C_1^2}\omega^2, \quad c_{12} = \frac{2C_2^2}{C_1^2}\gamma_2^2\sin^2\zeta_2 - \frac{\alpha_1}{C_1^2}\omega^2, \quad c_{13} = -\frac{C_2^2}{C_1^2}\gamma_3^2\sin(2\zeta_3),$$

$$c_{21} = -\gamma_1^2\sin(2\zeta_1), \quad c_{22} = -\gamma_2^2\sin(2\zeta_2), \quad c_{23} = \gamma_3^2\cos(2\zeta_3),$$

$$c_{31} = b_1, \quad , c_{32} = b_2, \quad , c_{33} = 0,$$

$$g_1 = -\frac{C_2^2}{C_1^2}\gamma_3^2\sin(2\zeta_0), \quad , g_2 = -\gamma_3^2\cos(2\zeta_0), \quad g_3 = 0.$$

Therefore, after applying Cramer's rule, the amplitude ratio of reflected longitudinal wave, reflected thermal-mode wave and reflected transverse wave, i.e., $\frac{\mathfrak{A}_2}{\mathfrak{A}_5}$, $\frac{\mathfrak{A}_3}{\mathfrak{A}_5}$, and $\frac{\mathfrak{A}_4}{\mathfrak{A}_5}$ are obtained as follows:

$$Z_4 = \frac{\mathfrak{A}_2}{\mathfrak{A}_5} = \frac{D_1}{D}, \quad Z_5 = \frac{\mathfrak{A}_3}{\mathfrak{A}_5} = \frac{D_2}{D}, \quad Z_6 = \frac{\mathfrak{A}_4}{\mathfrak{A}_5} = \frac{D_3}{D}, \tag{3.3.25}$$

where,

$$D = c_{11}(c_{22}c_{33} - c_{23}c_{32}) - c_{12}(c_{21}c_{33} - c_{23}c_{31}) + c_{13}(c_{21}c_{32} - c_{22}c_{31}),$$

$$D_1 = g_1(c_{22}c_{33} - c_{23}c_{32}) - g_2(c_{12}c_{33} - c_{13}c_{32}) + g_3(c_{12}c_{23} - c_{13}c_{22}),$$

$$D_2 = -g_1(c_{21}c_{33} - c_{23}c_{31}) + g_2(c_{11}c_{33} - c_{13}c_{31}) - g_3(c_{11}c_{23} - c_{13}c_{21}),$$

$$D_3 = g_1(c_{21}c_{32} - c_{22}c_{31}) - g_2(c_{11}c_{32} - c_{12}c_{31}) + g_3(c_{11}c_{22} - c_{21}c_{12}).$$

3.4 Numerical Results and Discussion

In order to illustrate the theoretical results derived in the preceding sections, the present section is devoted to show the numerical results. For this purpose, magnesium crystal is considered as material of the medium with the following elastic and thermal constants at $T_0 = 298K$:

$$\lambda_0 = 2.17 \times 10^{10}\text{N m}^{-2},\ \ \mu_0 = 3.278 \times 10^{10}\text{N m}^{-2},\ \ K_0 = 1.7 \times 10^{2}\text{W m}^{-1}\text{K}^{-1},$$
$$\rho = 1.74 \times 10^{2}\text{kg m}^{-3} C_E = 1.04 \times 10^{3},\ \ , \beta_0 = 2.68 \times 10^{6}\text{N m}^{-2}\text{K}^{-1},\ \ \nu^2 = \frac{\lambda_0 + 2\mu_0}{\rho},$$
$$K_0^* = \frac{c_E(\lambda_0 + 2\mu_0)}{4},\ \ l = \frac{K}{\rho c_E\, \nu},$$

with non-dimensional phase-lags, $\tau = 0.1$ and $\tau_q = 0.2$.

With an objective of analyzing the reflection of thermoelastic waves at the boundary surface, the variation in absolute value of amplitude ratios is studied with respect to various incident angles under recently proposed theory by Quintanilla (2011). The numerical results for the four thermoelastic models considered here are plotted together which helps in highlighting the specific characteristics of reflected waves due to new thermoelastic theory of Quintanilla as compared to other existing theories of thermoelasticity. Different values of empirical material constant (α^*) are considered to mark the effects of temperature-dependent elastic parameters. Moreover, the nature of phase velocity for all the three waves is analyzed for different values of angular frequency (ω). The amplitude ratios and phase velocities for longitudinal elastic-mode, thermal-mode, and transverse elastic-mode waves are computed using a mathematical software, Mathematica 11.3.

Important findings under the case of incident longitudinal wave and incident transverse wave are discussed in Subsection 3.4.1 and Subsection 3.4.2, respectively, whereas Subsection 4.3 highlights about the variations in phase velocities of longitudinal elastic-

mode wave (V_1), thermal-mode wave (V_2), and transverse wave (V_3).

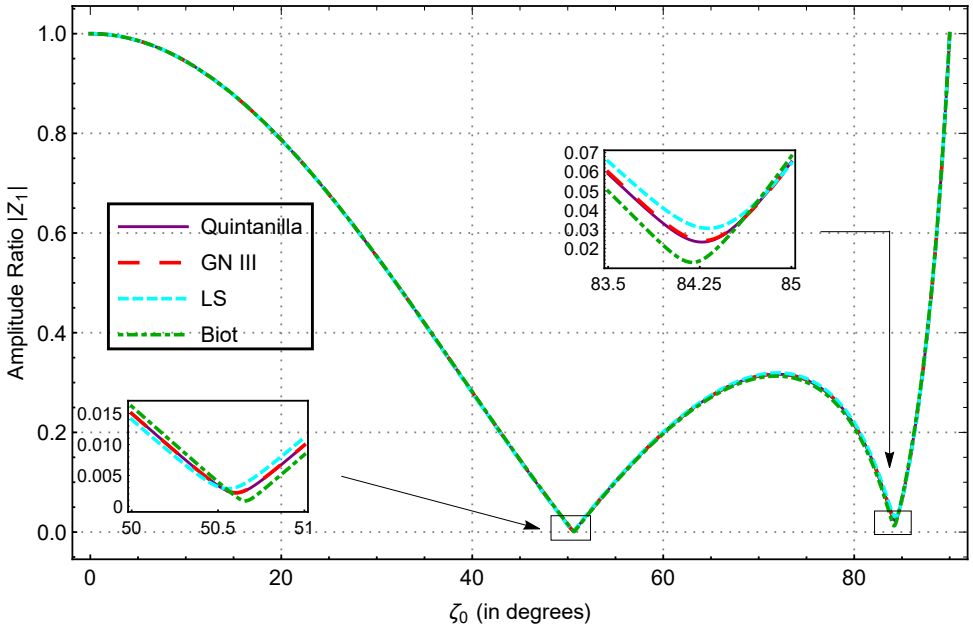

Figure 3.4.1: Distribution of $|Z_1|$ (Case A) for different theories with respect to angle of incident ζ_0, for $\alpha^* = 0.0002$ and $\omega = 1.5$

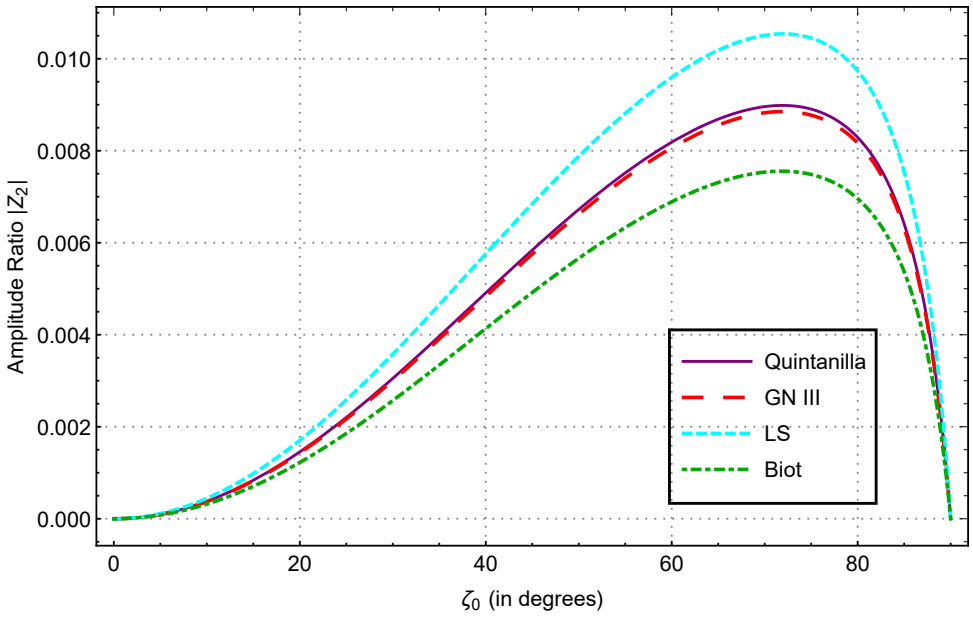

Figure 3.4.2: Distribution of $|Z_2|$ (Case A) for different theories with respect to angle of incident ζ_0, for $\alpha^* = 0.0002$ and $\omega = 1.5$

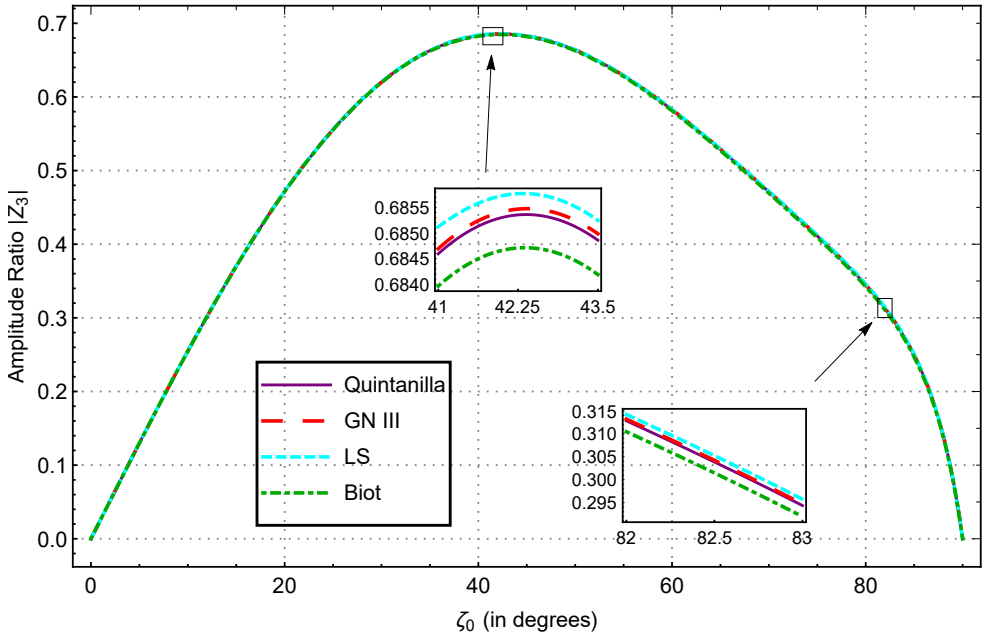

Figure 3.4.3: Distribution of $|Z_3|$ (Case A) for different theories with respect to angle of incident ζ_0, for $\alpha^* = 0.0002$ and $\omega = 1.5$

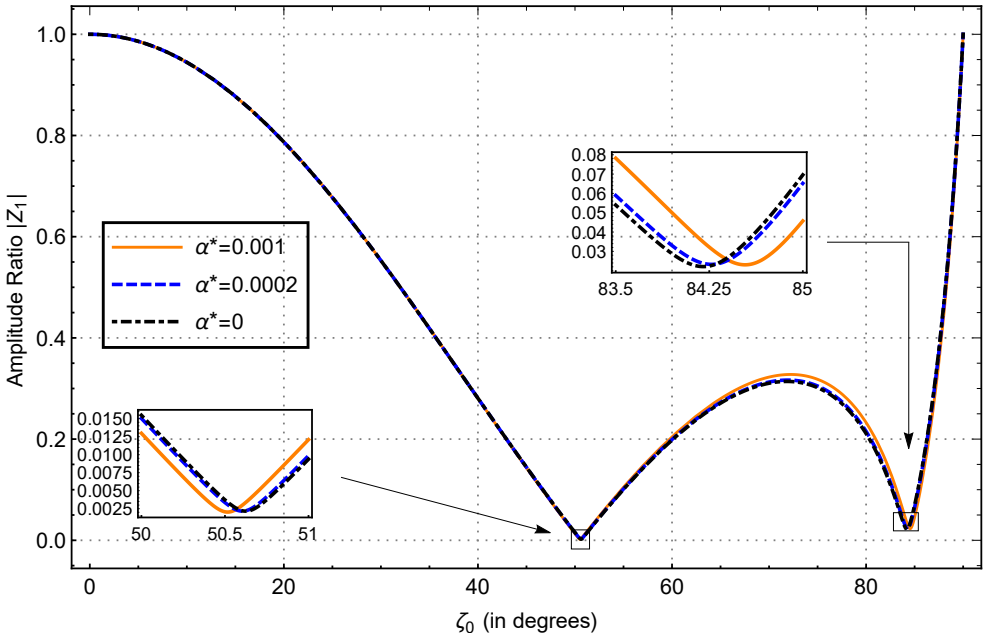

Figure 3.4.4: Distribution of $|Z_1|$ (Case A) for different values of empirical material constant (α^*) with respect to angle of incident ζ_0 with $\omega = 1.5$

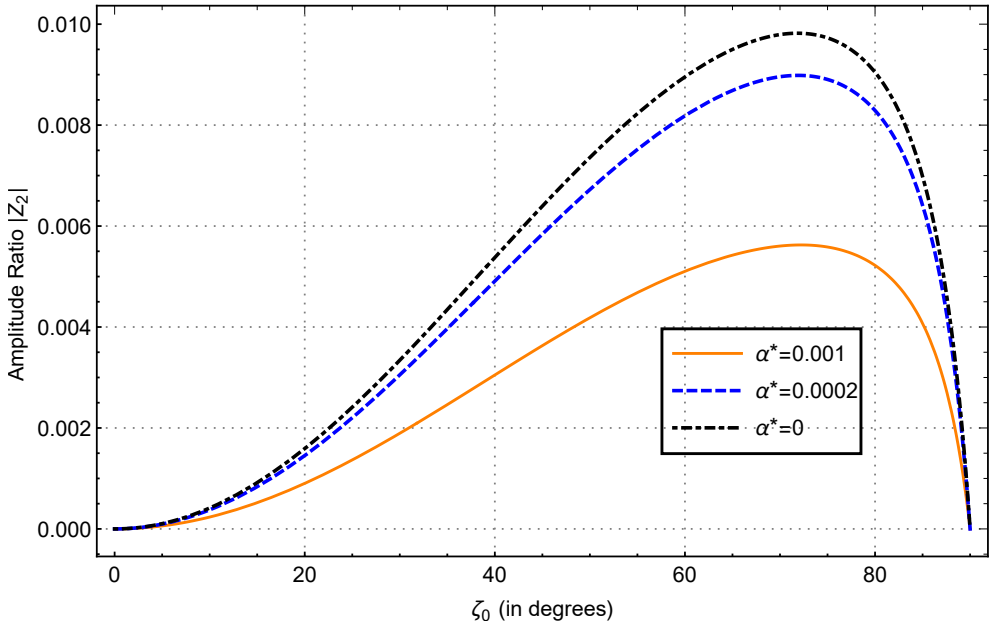

Figure 3.4.5: Distribution of $|Z_2|$ (Case A) for different values of empirical material constant (α^*) with respect to angle of incident ζ_0 with $\omega = 1.5$

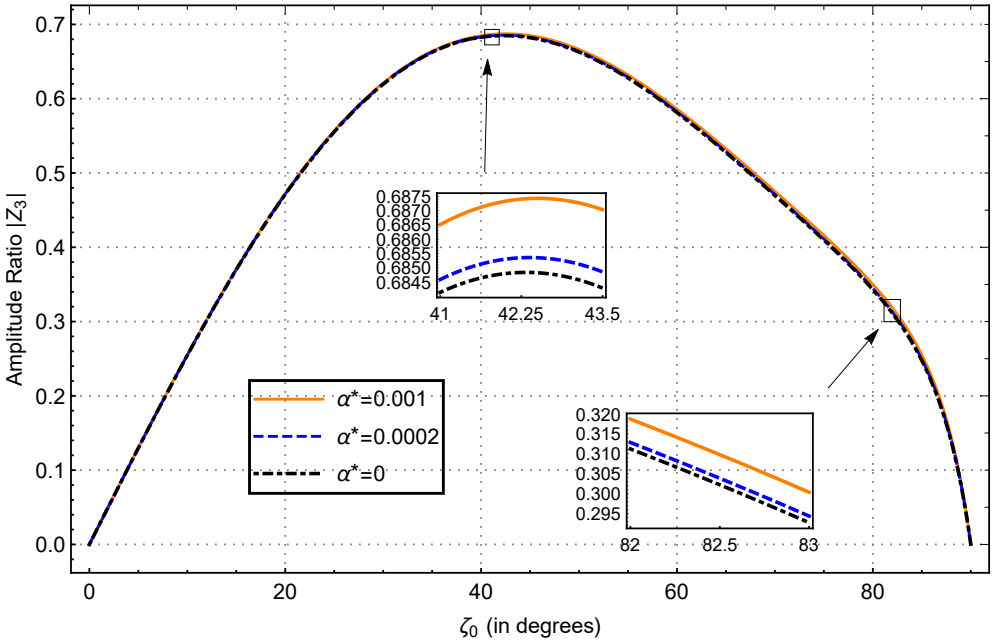

Figure 3.4.6: Distribution of $|Z_3|$ (Case A) for different values of empirical material constant (α^*) with respect to angle of incident ζ_0 with $\omega = 1.5$

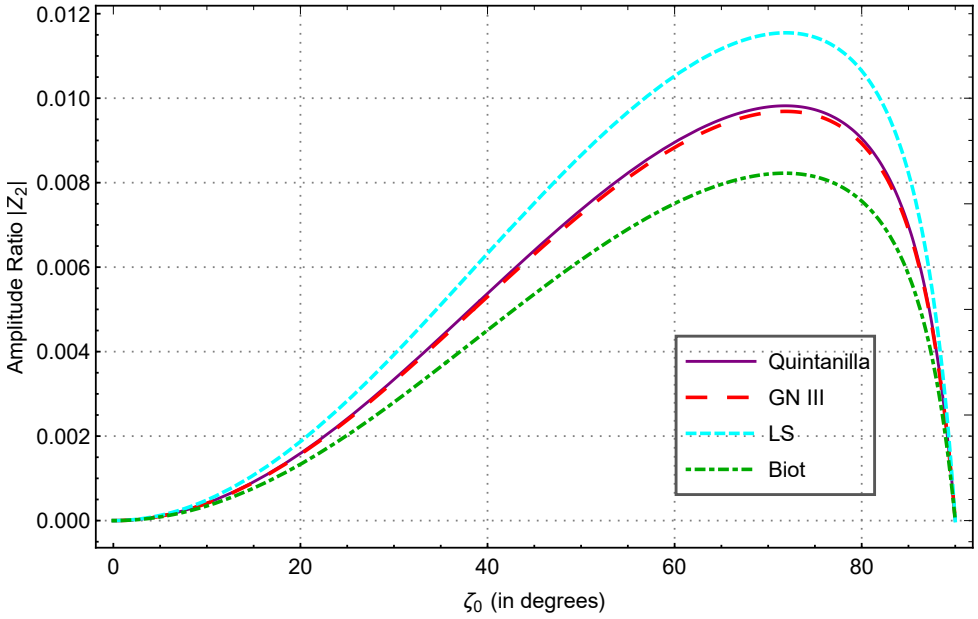

Figure 3.4.7: Another distribution of $|Z_2|$ (Case A) for different theories with respect to angle of incident ζ_0, for $\alpha^* = 0$ and $\omega = 1.5$

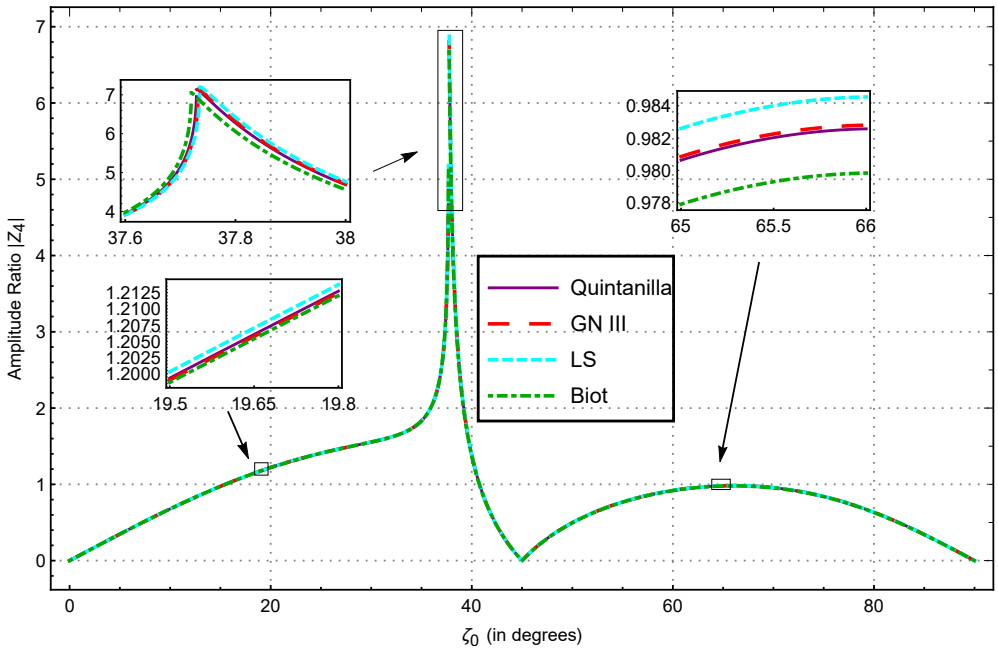

Figure 3.4.8: Distribution of $|Z_4|$ (Case B) for different theories with respect to angle of incident ζ_0, for $\alpha^* = 0.0002$ and $\omega = 1.5$

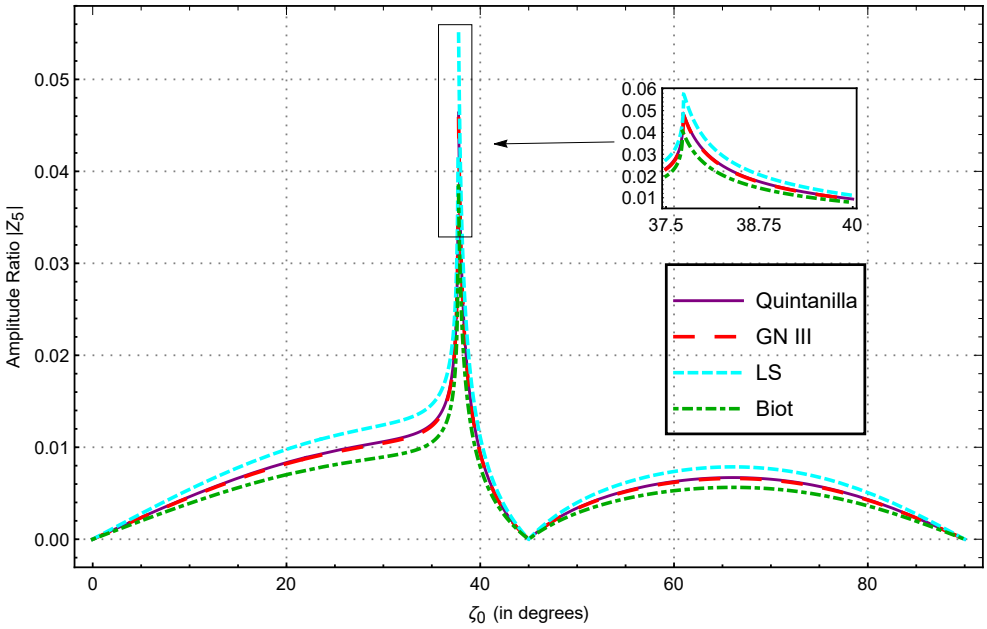

Figure 3.4.9: Distribution of $|Z_5|$ (Case B) for different theories with respect to angle of incident ζ_0, for $\alpha^* = 0.0002$ and $\omega = 1.5$

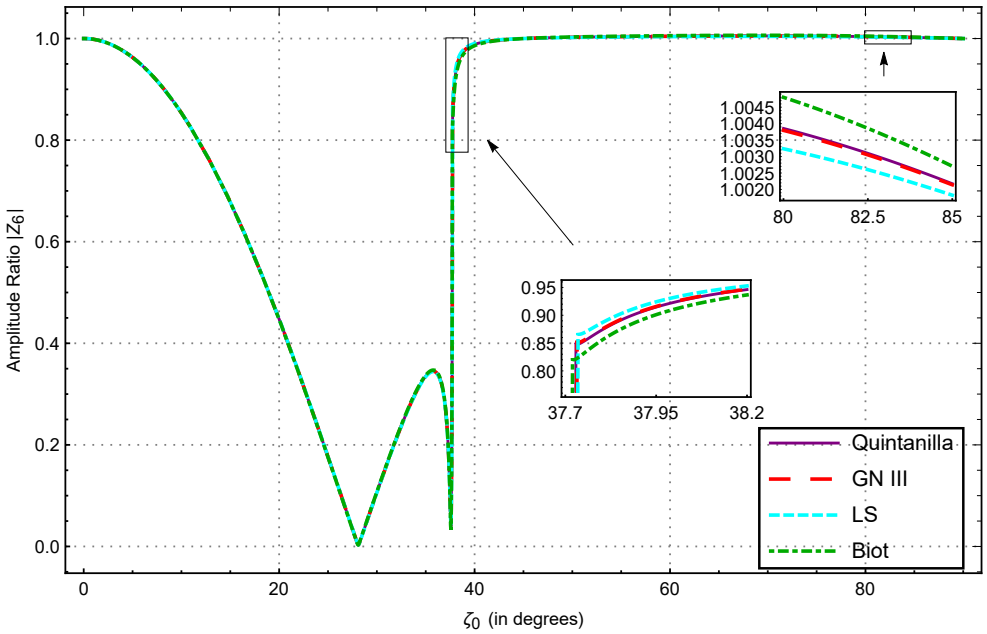

Figure 3.4.10: Distribution of $|Z_6|$ (Case B) for different theories with respect to angle of incident ζ_0, for $\alpha^* = 0.0002$ and $\omega = 1.5$

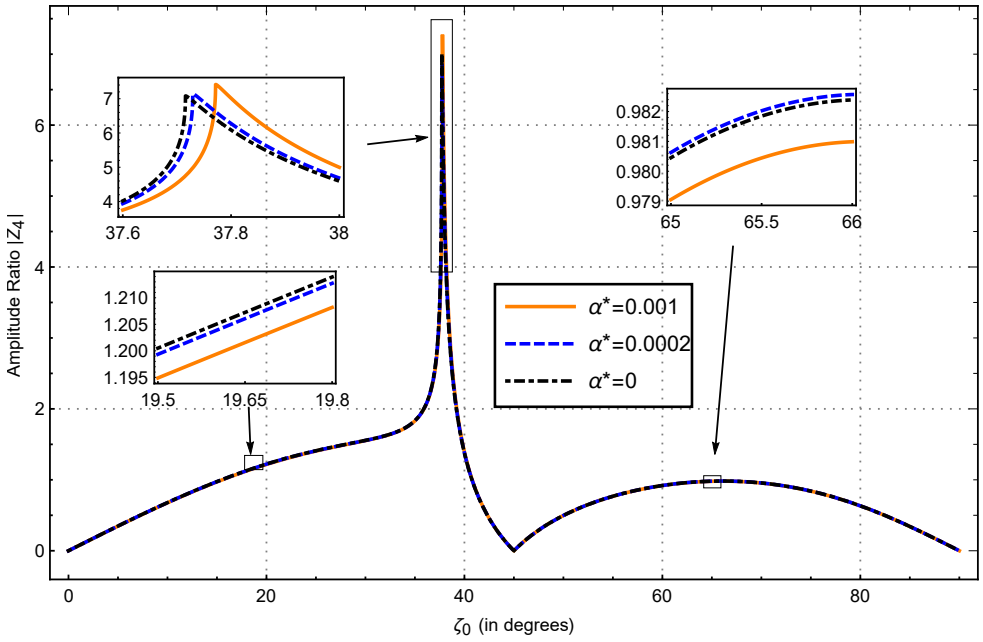

Figure 3.4.11: Distribution of $|Z_4|$ (Case B) for different values of empirical material constant (α^*) with respect to angle of incident ζ_0 with $\omega = 1.5$

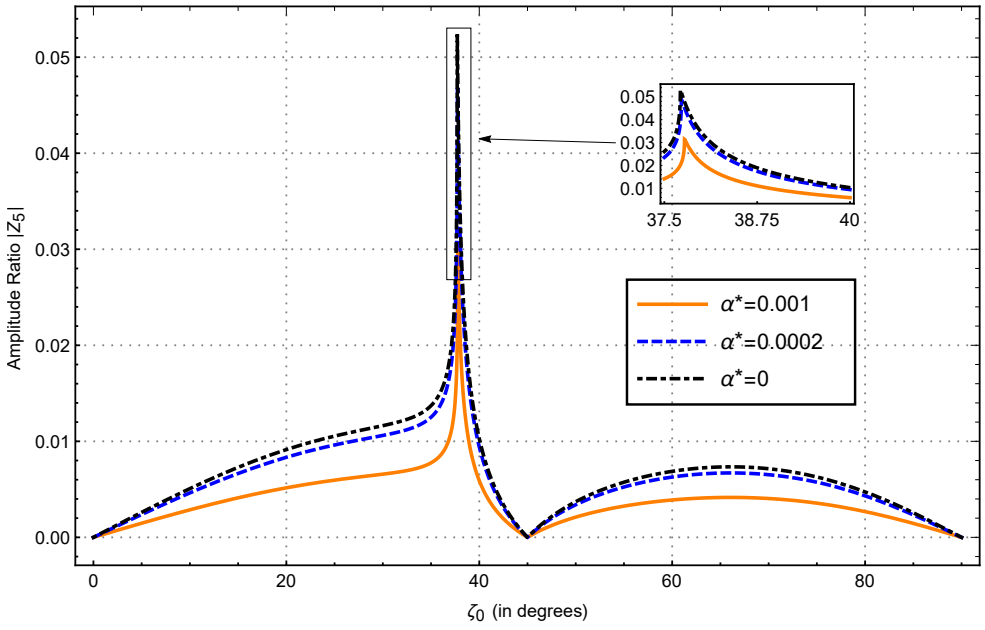

Figure 3.4.12: Distribution of $|Z_5|$ (Case B) for different values of empirical material constant (α^*) with respect to angle of incident ζ_0 with $\omega = 1.5$

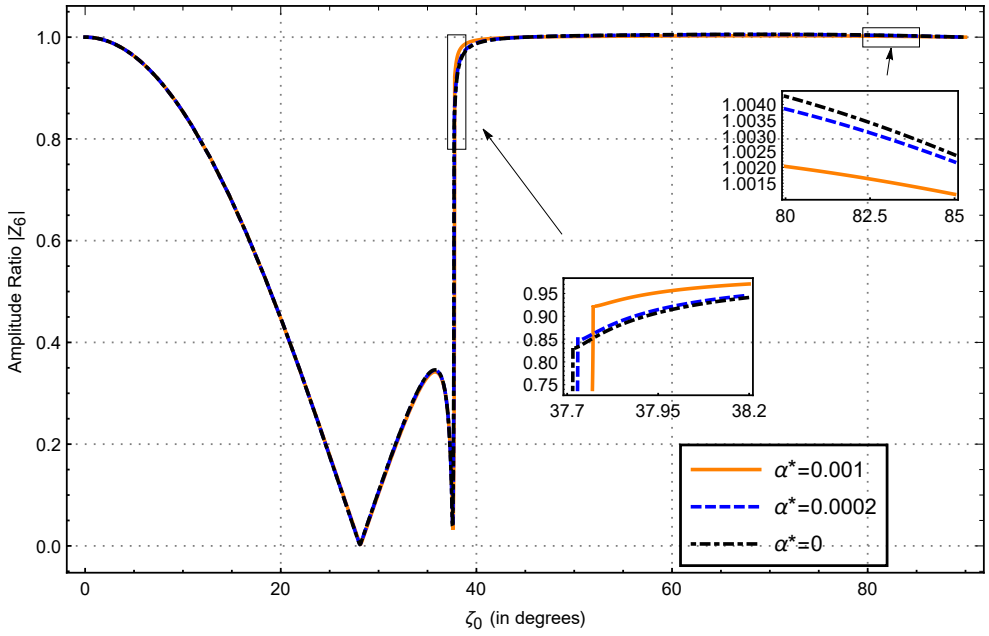

Figure 3.4.13: Distribution of $|Z_6|$ (Case B) for different values of empirical material constant (α^*) with respect to angle of incident ζ_0 with $\omega = 1.5$

3.4.1 Case A: Results for Incident Longitudinal Wave

For the case of incident longitudinal wave, the graphs for absolute value of amplitude ratios are plotted with respect to incidence angle (ζ_0) between 0^o and 90^o. Variations in amplitude ratios in the context of different thermoelasticity theories are shown in the Figs. (3.4.1-3.4.3) using dimensionless angular frequency (ω) = 1.5 and empirical material constant (α^*) = 0.0002. On the other hand, Figs. (3.4.4-3.4.6) show the variations due to different values of α^* for the considered model (Quintanilla's model) for $\omega = 1.5$.

Figure 3.4.1 depicts the behavior of absolute value of amplitude ratio ($|Z_1|$) for reflected longitudinal wave with respect to the incident angle (ζ_0) in the context of four thermoelasticity theories namely, Biot model, LS model, GN III model, and Quintanilla model. $|Z_1|$ starting with value 1 at incidence angle zero decreases to experience a local minimum at $\theta = 45^o$. Further, a local maximum is observed at 71.92^o for Quintanilla's model with another local minimum at $\zeta_0 = 84.27^o$ and then increases to

value 1 at 90°. There is a difference in prediction by different models. It is specifically noticeable that for $0^o \leq \zeta_0 \leq 50.54^o$ and $84.61^o \leq \zeta_0 \leq 90^o$, the values of $|Z_1|$ are greater for the Biot model in comparison to the other models, whereas for the middle range, i.e., for $50.54^o < \zeta_0 < 84.61^o$, the higher values are acquired by LS model. It is apparent from the Fig. 3.4.1 that the values for Quintanilla and GN III model mostly lie between the values for LS and Biot model for longitudinal wave. This behavior suggests the significant effect of phase-lag, τ_q and the material parameter, K^* (conductivity rate). It is further appropriate to point out that the effect of delay time, τ is minute as the amplitude ratio for longitudinal wave in case of Quintanilla model and GN III is approximately the same. Quintanilla model and GN III model acquire local minima for angle of incidence $\zeta_0 = 50.60^o$ and $\zeta_0 = 84.27^o$ with values $0.00216, 0.00220$ and $0.02326, 0.02399$, respectively. On the other hand, LS theory predicts a local minima at $\zeta_0 = 50.56^o, 84.32^o$ with values $0.00284, 0.03045$ and Biot theory shows the local minima at $\zeta_0 = 50.66^o, 84.19^o$ with values $0.00089, 0.01264$, respectively. For local maxima, four thermoelasticity models, Biot model, LS model, GN III model, and Quintanilla model attain at $\zeta_0 = 71.83^o, 71.98^o, 71.93^o,$ and 71.92^o with values $0.31294, 0.31928, 0.31703$, and 0.31661, respectively. This implies a significant difference in predictions of maximum and minimum peaks by different models, although the prediction by new model mostly agrees with the prediction by GN-III model.

The variation of absolute value of amplitude ratio ($|Z_2|$) for reflected thermal-mode wave with respect to the incident angle (ζ_0) is shown in Fig. 3.4.2. It presents the variation in the values for Biot, LS, GN III, and Quintanilla thermoelasticity model and indicates a significant difference in the prediction of results by different theories. $|Z_2|$ increases from zero to attain local maximum and then decreases to zero. This means that when longitudinal elastic-mode wave falls at surface ($z = 0$), making angle 0^o and 90^o with z axis, then only the longitudinal elastic-mode wave is reflected back. Furthermore,

according to this figure, it is revealed that in the context of LS model, $|Z_2|$ acquires higher values, whereas Biot model attains the lower values for $0^o \leq \zeta_0 \leq 90^o$, in comparison to other models. The amplitude ratio for thermal-mode wave in case of Quintanilla model and GN III model always lies between the values for Biot and LS model. However, the values of $|Z_2|$ for Quintanilla model are greater in comparison to GN III theory which points out the effect of delay time, τ. It is also observed that all four thermoelasticity theories show a local maximum of the field and that is acquired by Quintanilla model, GN III model, LS model, and Biot model at $\zeta_0 = 71.91^o, 71.92^o, 71.96^o,$ and 71.83^o with maximum value of $0.00898, 0.00885, 0.01054,$ and 0.00755, respectively.

Figure 3.4.3 demonstrates the nature of absolute value of amplitude ratio ($|Z_3|$), for all the considered thermoelasticity theories in the context of reflected transverse wave, with respect to incident angle (ζ_0). Similar to thermal-mode wave, the absolute value of reflection coefficient starts with zero at zero incidence angle and ends with zero after attaining a local maximum. This implies that neither of reflected thermal-mode wave and reflected elastic-mode transverse wave is observed at incidence angles, 0^o and 90^o. The values for LS model are higher throughout in comparison to other models whereas Biot thermoelasticity model takes the smallest values. Values for Quintanilla and GN III thermoelasticity model lie between the values for Biot and LS model with values for GN III slightly greater than that of Quintanilla model. For $|Z_3|$, the time lag, τ reduces the values which is opposite to the case of $|Z_2|$. Similar to case of $|Z_2|$, one local maxima is observed with no local minima. Quintanilla theory and GN III theory acquire local maxima at approximately $\zeta_0 = 42.39^o$ with values 0.68536 and 0.68547, respectively. Further, LS and Biot theories acquire local maxima at $\zeta_0 = 42.33^o, 42.36^o$ with values $0.68577, 0.68471$, respectively. However, the disagreement of different theories for predicting the amplitude ratio $|Z_3|$ is not very prominent as compared to the case of $|Z_2|$.

Figures (3.4.4-3.4.6) highlight the differences in the absolute values of amplitude

ratio for reflected longitudinal wave, thermal-mode wave, and transverse wave, respectively in the context of Quintanilla thermoelasticity theory for various values of empirical material constant (α^*). These figures help to understand the effects of temperature-dependent elastic material when longitudinal elastic-mode wave falls at the boundary.

From Fig. 3.4.4, the effects of change in value of α^* are observed more significantly for $50.57^o < \zeta_0 \leq 84.31^o$ in comparison to other incident angle for the case of reflected longitudinal wave. For $50.57^o < \zeta_0 \leq 84.31^o$, the absolute values decrease with the decrease in values of α^*. On the other hand, for $40.73^o < \zeta_0 \leq 50.57^o$ and $84.41^o < \zeta_0 \leq 90^o$, the absolute values increase with a decrease in values of α^* while no specific trend is observed for remaining angles. Slight shifts in local maxima and minima are detected. Local minima for $\alpha^* = 0.001$ are attained at $\zeta_0 = 50.52^o$ and $\zeta_0 = 84.54^o$ whereas for $\alpha^* = 0$, local minima are attained at $\zeta_0 = 50.62^o$and $\zeta_0 = 84.20^o$. Hence, the first local minima shift to left with minute decrease in values as α^* increases. Similarly, the local maximum for $\alpha^* = 0.001$ is obtained at $\zeta_0 = 72.22$ with value 0.32773 while for $\alpha^* = 0$, it is obtained at $\zeta_0 = 71.85^o$ with value 0.31395. Therefore, it can be stated that the local maxima shift right with increase in values as α^* increases.

The variations in absolute values of amplitude ratio due to different values of empirical material constant (α^*) for reflected thermal-mode wave are recorded in the Fig. 3.4.5. It is observed that the with the increase in values of α^*, $|Z_2|$ decreases significantly. Right shift in local maximum is detected with increase in the value of α^*. Local maximum is obtained at $\zeta_0 = 71.84^o$, 71.91^o, and 72.21^o for $\alpha^* = 0$, 0.0002, and 0.001 with values $0.00982, 0.00898,$ and 0.00563, respectively.

Figure 3.4.6 reveals the changes in nature of absolute values of amplitude ratio for reflected transverse wave when the values of α^* are changed. In contrast to thermal-mode wave, for reflected transverse wave, the absolute value of amplitude ratio ($|Z_3|$) decreases with decrease in value of empirical material constant (α^*) for $0^o \leq \zeta_0 \leq 90^o$. It is also observed that there is a slight right shift in local maximum as value of α^*

increases. The local maxima shifts from $\zeta_0 = 42.32^o$ to $\zeta_0 = 42.5^o$ as value of α^* increases from 0 to 0.001. This implies that the maximum value of this ratio is attained for higher angle of incidence with an increase in parameter α^*.

Further, in an attempt to analyze the effect of empirical material constant (α^*) due to different theories, a graph is plotted for variation in $|Z_2|$ versus incident angle for $\alpha^* = 0$ as shown in Fig. 3.4.7. On comparison of this figure with Fig. 3.4.2, it is observed that the change in value of α^* has no specific effect on applying any particular theory. Hence, the graphs are plotted only in the context of the new theory (Quintanilla's theory) to analyze the variation of empirical material constant.

3.4.2 Case B: Results for Incident Transverse Wave

The variations in the absolute values of amplitude ratio for three different reflected waves in the case of incident transverse wave can be observed from the Figs. (3.4.8-3.4.13). In order to show the comparison between four considered theories for incident transverse wave, graphs are shown in Figs. (3.4.8-3.4.10) for $\alpha^* = 0.0002$ and $\omega = 1.5$ whereas changes due to different values of α^* are presented in Figs. (3.4.11-3.4.13) for $\omega = 1.5$.

Figure 3.4.8 depicts the variations in absolute values of amplitude ratio ($|Z_4|$) for reflected longitudinal wave in the context of all four thermoelasticity theories. Unlike Case A, the variation in amplitude ratio for reflected longitudinal elastic-mode wave experiences peak when incidence angle (ζ_0) is 37.74^o for Quintanilla's model. The amplitude ratio of reflected wave in this case is zero at $\zeta_0 = 0^o$ and 90^o which suggests that the transverse wave is reflected back completely at these angle of incidence. It is further observed that the values of $|Z_4|$ are larger in case of LS model for the range $0^o \leq \zeta_0 \leq 36.8^o$ and $37.74^o \leq \zeta_0 \leq 90^o$ and in case of Biot model for $36.8^o < \zeta_0 < 37.74^o$. The nature of graphs for all thermoelasticity models are same but the values given by different theories vary. Each thermoelasticity theory witnesses the highest

value, the lowest value, and a local maximum. The highest point is attained at $\zeta_0 = 37.72^o, 37.73^o, 37.74^o$, and 37.74^o for Biot model, Quintanilla model, LS model, and GN III model, respectively with LS model acquiring the highest value of 7.17225. One local maximum is attained at the incident angle, $\zeta_0 = 66.07^o$ in case of all considered theories. All the four theories show the lowest value, 0 at $\zeta_0 = 45^o$. Absolute values of amplitude ratio for Quintanilla theory and GN III theory lie between the values of Biot and LS theory. With a comparison between Quintanilla and GN III model, GN III model shows the higher values in the range of incident angle $0^o \leq \zeta_0 \leq 37.73^o$ whereas Quintanilla model acquires higher values otherwise. This shows the effect of delay time, τ. However, similar to the Case A, the effect of delay time, τ is less in comparison to thermal conductivity rate, K^* and phase-lag, τ_q.

Differences in the absolute values of amplitude ratio ($|Z_5|$) for reflected thermal-mode waves for four different thermoelasticity theories are presented in the Fig. 3.4.9. Unlike Case A, the nature of thermal-mode wave and longitudinal elastic-mode wave is same in Case B. In this case also, reflection coefficient (Z_5) experiences peak at $\zeta_0 = 37.74^o$ for Quintanilla's model. Neither of longitudinal elastic-mode wave nor thermal-mode wave is reflected when transverse wave falls at surface with $\zeta_0 = 0^o$ and 90^o. It is further evident that LS thermoelasticity model acquires higher absolute values of this amplitude ratio for all incident angles between 0^o and 90^o whereas Biot model shows lower values, in comparison to other models. Relative to GN III model, Quintanilla model attains greater values in this scenario for all incident angles. LS theory takes the highest absolute value of 0.05731 for $|Z_5|$ at 37.74^o whereas Biot model acquires 0.04059 as highest value at incident angle, $\zeta_0 = 37.72^o$. Similarly, Quintanilla and GN III model attain the highest value of 0.04873 and 0.04759, respectively at approximately $\zeta_0 = 37.74^o$. Another local maximum is attained for all thermoelasticity theories at $\zeta_0 = 66.07^o$ similar to $|Z_4|$. The lowest value of 0 is attained by all the four theories at $\zeta_0 = 45^o$.

Figure 3.4.10 shows the variations of the absolute value of reflection coefficient ($|Z_6|$) of reflected transverse wave for all the four thermoelasticity theories in the context of incident transverse wave. The significant change is observed in nature of amplitude ratio for reflected transverse wave in comparison to Case A. The amplitude ratio experiences a local minimum and two local maxima. In comparison to other models, the higher absolute values of Z_6 are acquired by LS thermoelasticity model in the incident angle range, $0^o \leq \zeta_0 < 28.09^o$, $37.47^o \leq \zeta_0 < 37.59^o$, and $45^o < \zeta_0 \leq 57.65^o$, by Biot model when $28.10^o \leq \zeta_0 \leq 37.32^o$, $37.60^o \leq \zeta_0 \leq 37.73^o$, and $45.1^o \leq \zeta_0 \leq 90^o$ and by GN III model otherwise. In general, values for Quintanilla and GN III remains in between the values for Biot and LS theories with Quintanilla taking greater values for the most incident angles between 0^o and 90^o, in comparison to GN III model. The maximum values of 1.00515 and 1.00507 for $|Z_6|$ are attained by Quintanilla and GN III model, respectively at approximate incident angle of 69.4^o. On the other hand, Biot model shows maximum value of 1.00642 at $\zeta_0 = 69.38^o$ and LS model predicts maximum value of 1.00432 at $\zeta_0 = 69.41^o$. The minimum value of $|Z_6|$ is attained by all four thermoelasticity models at approximately $\zeta_0 = 28.1$ with LS model attaining the least value of 0.00308.

The variation in the absolute values of amplitude ratio for reflected longitudinal wave, thermal-mode wave and transverse wave are featured in the Figs. (3.4.11-3.4.13), respectively in the context of Quintanilla thermoelasticity model, when various values of empirical material constant (α^*) are considered for $\omega = 1.5$.

From Fig. 3.4.11, it is observed that the temperature dependence of elastic parameters has significant impact on the amplitude ratio of reflected longitudinal wave ($|Z_4|$), when transverse wave falls at the boundary surface. It is noticed that for incidence angle (ζ_0) between 37.72^o and 90^o, $|Z_4|$ attains higher values when empirical material constant is non zero ($\alpha^* \neq 0$). However, when the elastic parameters are independent of temperature (i.e. $\alpha^* = 0$), $|Z_4|$ attains higher values for $0^o \leq \zeta_0 \leq 37.72^o$. A slight right

shift from 37.72° to 37.78° is observed in the incidence angle at which peak is attained, when α^* changed from 0 to 0.001. However, impact of this effect on local minimum of $|Z_4|$ is noted to be negligible. $|Z_4|$ acquires the least value of zero at $\zeta_0 = 45°$ for all three values of empirical material constant.

The variations in absolute values of amplitude ratio ($|Z_5|$) due to different values of α^* for reflected thermal-mode wave are recorded in the Fig. 3.4.12. Similar to the Case A, with increase in values of α^*, amplitude ratio for reflected thermal-mode wave decreases significantly for any incidence angle between 0° and 90°. A right shift in the peak point is detected as the value of α^* is increased. Similar to reflected longitudinal wave, no impact of variation in α^* is noticed on the local minimum value for reflected thermal-mode wave. On the other hand, the values of $|Z_5|$ decrease with increase in value of empirical material constant at $\zeta_0 = 66.07°$. That is maximum value decreases with increase in value of α^*.

Changes in absolute values of amplitude ratio ($|Z_6|$) for reflected transverse wave with the variation in empirical material constant are shown in Fig. 3.4.13. Similar to Case A, the variations in amplitude ratio of reflected transverse wave due to temperature-dependent elastic parameter is lesser in comparison to other reflected waves. It is observed that for most of the incidence angles between 0° and 90°, the value of $|Z_6|$ is higher when $\alpha^* = 0$ as compared to values for $\alpha^* \neq 0$. With the increase in α^*, maximum value decreases significantly with small right shift in incident angle at which it is attained. Unlike other cases, there is an effect of change in α^* on the minimum value in this case. With increase in value of α^*, a right shift in local minimum is observed.

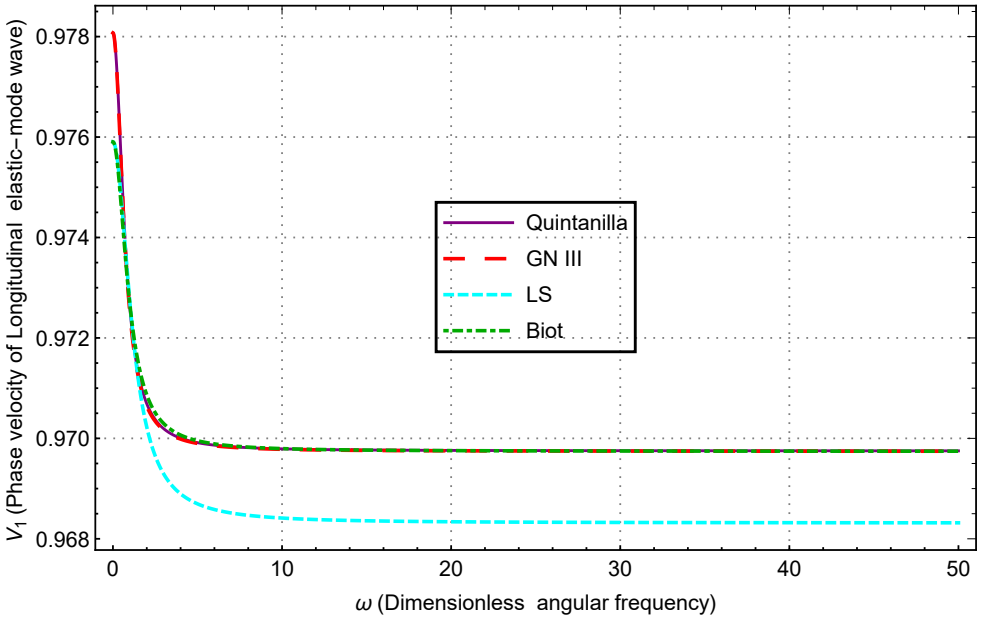

Figure 3.4.14: Distribution of longitudinal elastic-mode wave phase velocity (V_1) for different thermoelasticity theories with respect to dimensionless angular frequency (ω) with $\alpha^* = 0.0002$

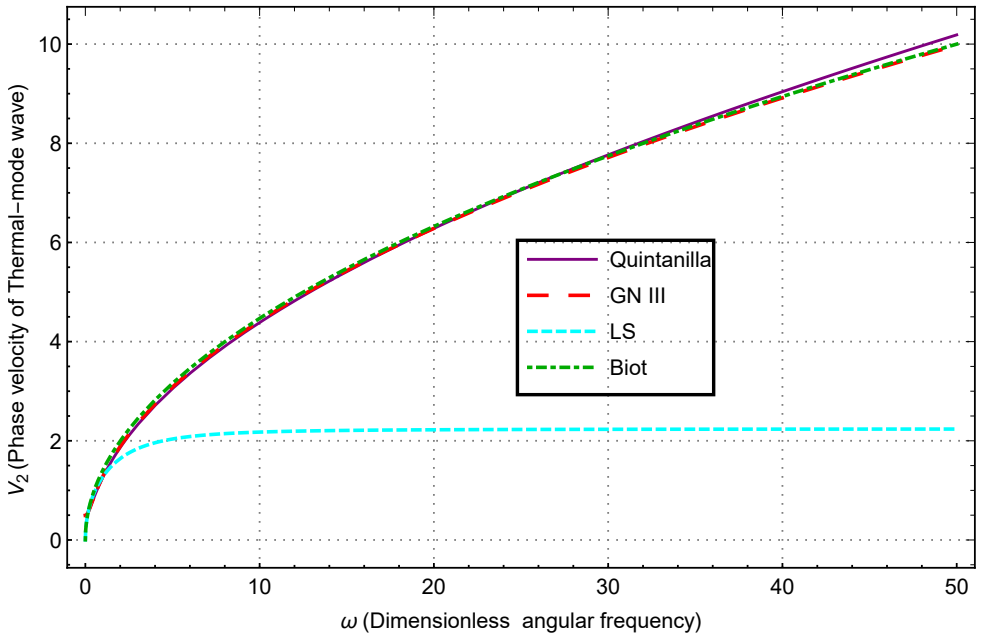

Figure 3.4.15: Distribution of thermal-mode wave phase velocity (V_2) for different thermoelasticity theories with respect to dimensionless angular frequency (ω) with $\alpha^* = 0.0002$

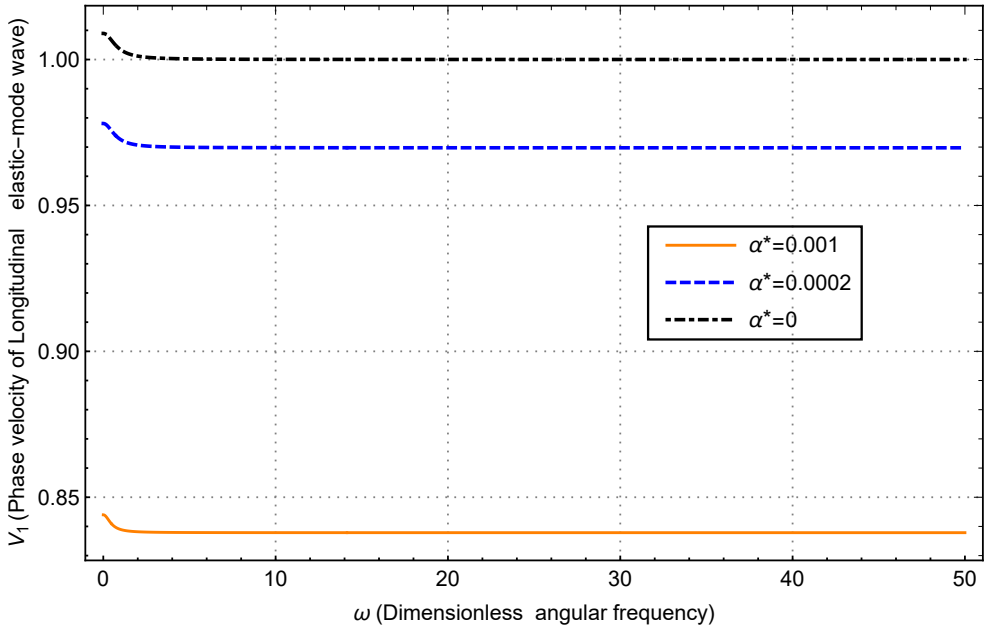

Figure 3.4.16: Distribution of longitudinal elastic-mode wave phase velocity (V_1) for different values of empirical material constant (α^*) with respect to dimensionless angular frequency (ω)

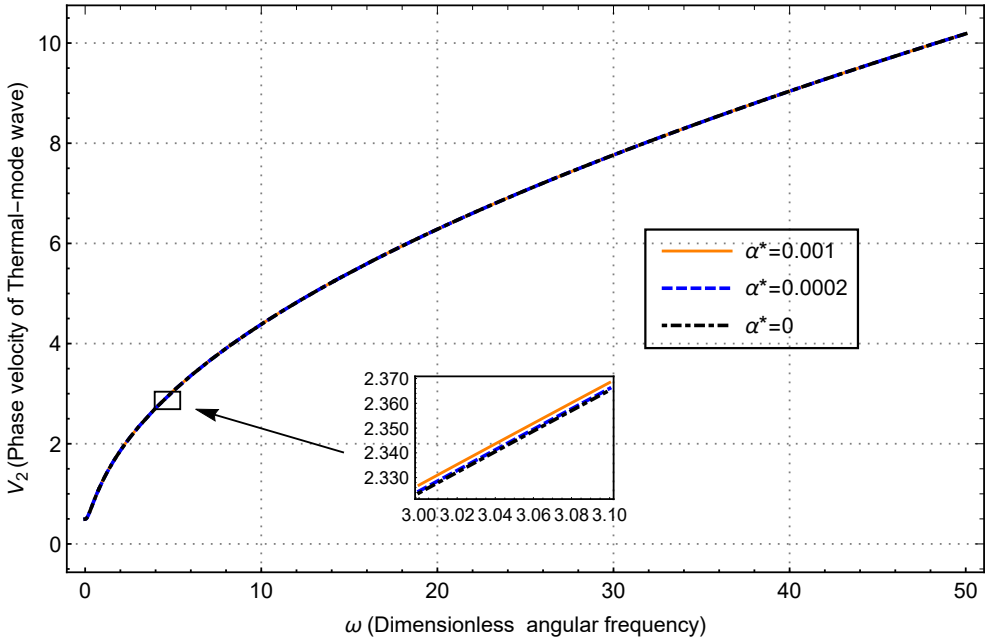

Figure 3.4.17: Distribution of thermal-mode wave phase velocity (V_2) for different values of empirical material constant (α^*) with respect to dimensionless angular frequency (ω)

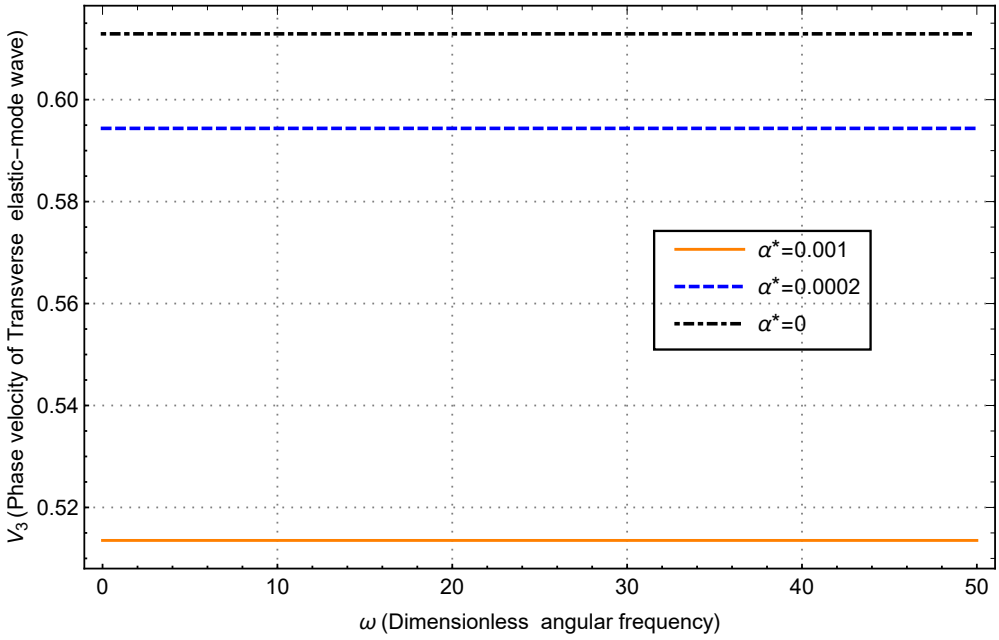

Figure 3.4.18: Distribution of transverse elastic-mode wave phase velocity (V_3) for different values of empirical material constant (α^*) with respect to dimensionless angular frequency (ω)

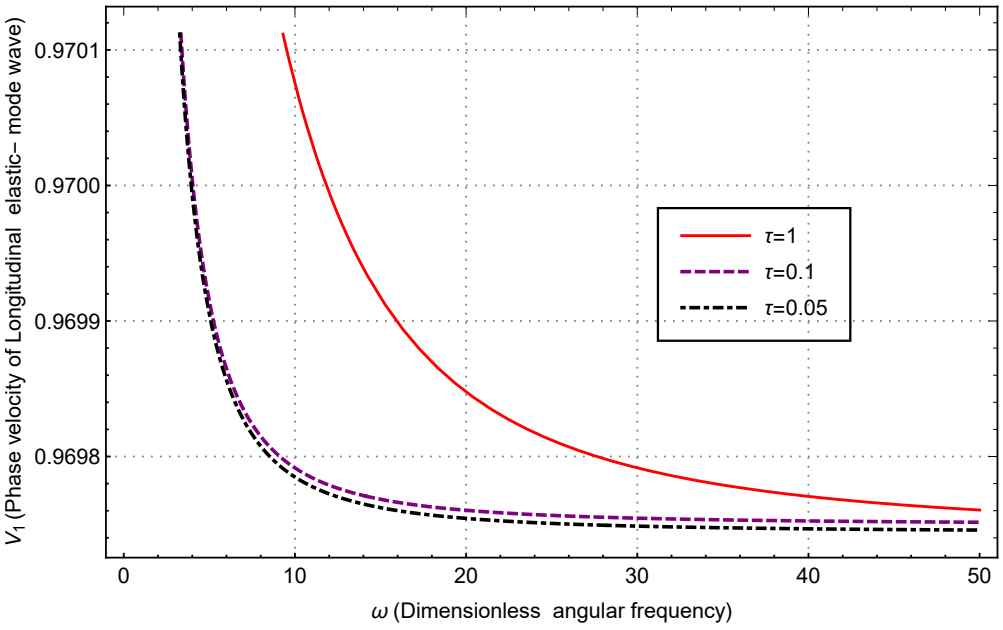

Figure 3.4.19: Distribution of longitudinal elastic-modewave phase velocity (V_1) for different values of delay time (τ) with respect to dimensionless angular frequency (ω) with $\alpha^* = 0.0002$

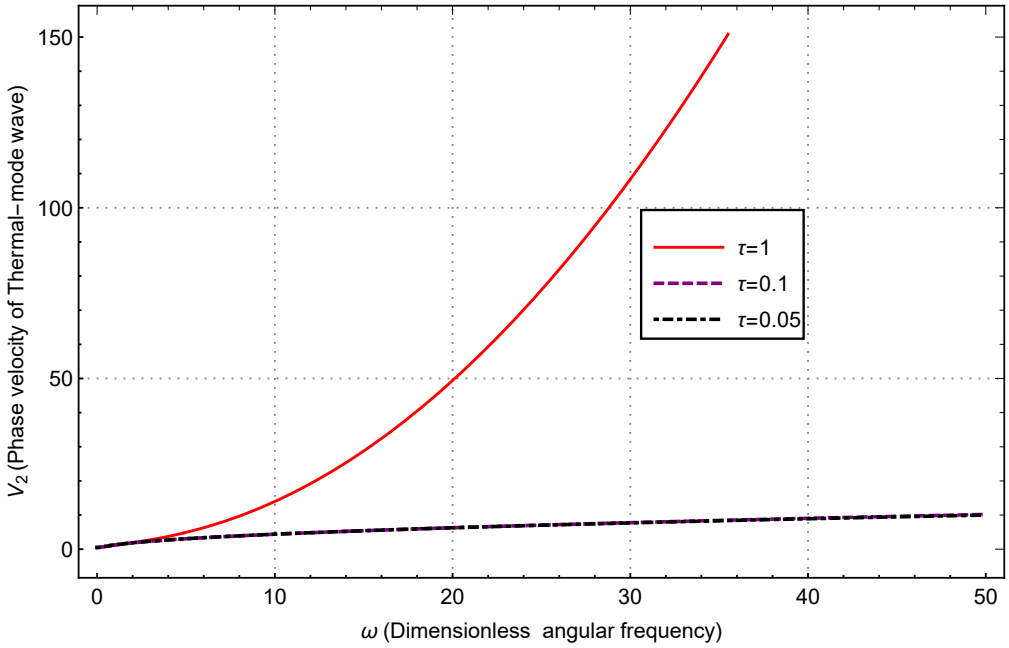

Figure 3.4.20: Distribution of thermal-mode wave phase velocity (V_2) for different values of delay time (τ) with respect to dimensionless angular frequency (ω) with $\alpha^* = 0.0002$

3.4.3 Variations in Phase Velocities

In this subsection, the effects on phase velocities of different types of waves due to various material parameter and thermoelasticity theories are observed. Figs. (3.4.14-3.4.15) show the variations of phase velocity of longitudinal wave (V_1) and thermal-mode wave (V_2) with respect to angular frequency (ω) for four thermoelasticity models namely, Biot model, LS model, GN III, and Quintanilla model for $\alpha^* = 0.0002$. The plots of phase velocity (V_3) of transverse wave are skipped as they are independent of τ and τ_q, therefore, it is predicted the same by all theories.

From Fig. 3.4.14, it is noticed that all four thermoelasticity theories attain finite phase velocity for longitudinal wave (V_1). However, the finite limiting value is different for different theories. For Quintanilla, GN III, and Biot model, V_1 approaches finite value of approximately 0.9697 whereas for LS model, phase velocity of longitudinal wave is 0.9683. On the other hand, V_1 for Quintanilla and GN III model acquires the same value of 0.9781 near $\omega = 0$ whereas the initial value of phase velocity for

longitudinal wave for LS and Biot model is 0.9759. Fig. 3.4.15 shows variations of phase velocity (V_2) for thermal-mode waves. From this figure, it is observed that except for LS model, thermal-mode phase velocity for other three models continuously increases as ω increases. On the other hand, thermal-mode phase velocity for LS model tends to the finite value of 2.169. This observation highlights the parabolic nature of thermoelasticity models: Biot, GN III, and Quintanilla. Fig. 3.4.15 also points out that rate of increase in values of V_2 is higher for Quintanilla model. From the Fig. 3.4.14, it is worth pointing out that the phase-lag, τ_q has significant effect on phase velocity for elastic-mode longitudinal wave in case of higher frequencies whereas the impact of K^* is prominently visible for lower range of frequencies. However, the involvement of delay time, τ in Quintanilla model does not alter the infinite speed behavior of thermal-mode wave in case of GN III (see Fig. 3.4.15). This is an important observation of present investigation.

Figures (3.4.16-3.4.18) present the variations of phase velocities with respect to dimensionless angular frequency (ω) for different values of α^* in the context of Quintanilla model. The observations are made by keeping τ fixed to 0.1 with α^* taking values 0, 0.0002, and 0.001. It is noticed that with the increase in values of α^*, the values of phase velocities for longitudinal and transverse wave (Fig. 3.4.16 and Fig. 3.4.18) decrease significantly without affecting the trend of variation. On the other hand, the change in values of α^* has minute effect on phase velocity of thermal-mode wave (Fig. 3.4.17).

The variations of phase velocities with respect to dimensionless angular frequency (ω) for different values of delay time, τ in the context of Quintanilla model are shown in Figs. (3.4.19-3.4.20). The graph of phase velocity for transverse wave (V_3) in this scenario is skipped as V_3 is independent of τ. The values for τ are considered as 0.05, 0.1, and 1 while keeping value of α^* fixed to 0.0002. V_1 is observed to increase with the increase in value of τ. On the other hand, the value of V_2 increases with the

decrease in values of τ for the angular frequency range of $0 \leq \omega \leq 1.86$ whereas for higher ω, values of V_2 increase drastically for $\tau = 1$.

3.5 Conclusion

In the present chapter, the reflection of thermoelastic waves in an isotropic medium with temperature dependent elastic properties under Quintanilla's thermoelasticity theory (Quintanilla (2011)) is investigated. The progression of reflected longitudinal and transverse wave, and reflected thermal-mode wave is traced for two cases, namely, incident longitudinal wave and incident transverse wave. In order to serve the above mentioned aim and to make a comparison with previously established theories, a combined system of field equations has been considered for four thermoelasticity theories: Biot, LS, GN III, and Quintanilla theories. The analytic expressions for phase velocities and amplitude ratios for reflected waves in both cases of reflection have been articulated. The behavior of reflected waves has been illustrated graphically by plotting absolute amplitude ratios of different reflected waves for both the cases. Further, a detailed analysis of the nature of reflected waves in Quintanilla's model is carried out by plotting amplitude ratios of different reflected waves for four thermoelastic models and for different values of non-homogeneity index parameter, α^*. Lastly, numerical results for phase velocities for all three waves are represented graphically in the context of different theories, different values of α^*, and different values of delay time parameter, τ. Through the analysis of results under present investigation, the following important observations can be summarized:

- In accordance with the comparative study, the reflection of thermoelastic waves is approximately of the same nature in case of Quintanilla and GN III theories. On the other hand, a notable difference in prediction of Quintanilla model is observed in comparison to Biot model and LS model. This trend highlights the significance of effect of thermal conductivity rate, K^* and phase-lag, τ_q over delay parameter,

τ.

- The empirical material constant, α^* significantly effects the progression of all the three reflected waves in the context of amplitude ratio and phase velocity. Also, the change in magnitude varies for different waves.

- The phase velocities of longitudinal elastic-mode wave and thermal-mode wave are highly effected by thermal conductivity rate and phase-lags. However, the phase velocity of transverse elastic-mode wave is only affected with the variation of non-homogeneity index parameter, α^*. This implies that temperature-dependent elastic material significantly affects the thermoelastic wave progression.

- Present analysis of phase velocity profiles indicates that the Quintanilla model still suffers from the paradox of infinite speed of thermal-mode longitudinal wave propagation like GN III theory and Biot's theory. However, LS theory accounts for the finite speed for both the elastic-mode longitudinal wave as well as of thermal-mode longitudinal wave and demonstrates the hyperbolic nature of the model.